

The impact of medium-width bands on the selection, and subsequent luminosity function measurements, of high- z galaxies

N. J. Adams^{1*}, D. Austin,¹ T. Harvey,¹ C. J. Conselice,¹ J. A. A. Trussler,² Q. Li,¹ L. Westcott,¹ L. Ferreira,³ V. Rusakov,¹ C. M. Goolsby,¹

¹*Jodrell Bank Centre for Astrophysics, University of Manchester, Oxford Road, Manchester, UK*

²*Center for Astrophysics | Harvard & Smithsonian, 60 Garden St., Cambridge MA 02138 USA*

³*School of Physics and Astronomy, University of Victoria, Victoria, BC, Canada*

Accepted XXX. Received YYY; in original form ZZZ

ABSTRACT

New, ultra-deep medium-width photometric coverage with JWST’s NIRC*am* instrument provides the potential for much improved photo- z reliability at high redshifts. In this study, we conduct a systematic analysis of the JADES Origins Field, which contains 14 broad- and medium-width near-infrared bands, to assess the benefits of medium band photometry on high- z sample completeness and contamination rates. Using imaging with depths of AB mag 29.8 – 30.35, we conduct an experiment to observe how high- z selections differ when images are artificially degraded or bands are removed. In parallel, the same experiments are conducted on simulated catalogues from the JAGUAR semi-analytic model to examine if the behaviour from observations can be replicated. We find sample completeness is high (80%+) and contamination low (< 4%) when in the $10\sigma+$ regime, even without the use of any medium-width bands. The addition of medium-width bands leads to notable increases in completeness ($\sim 10\%$) but multiple bands are required to improve contamination rates due to the small redshift ranges over which they probe strong emission lines. Incidents of Balmer-Lyman degeneracy increase in the $5 - 7\sigma$ regime and this can be replicated in both simulated catalogues and degraded real data. We measure the faint-end of the UV LF at $8.5 < z < 13.5$, finding high number densities that agree with previous JWST observations. Overall, medium bands are effective at increasing completeness and reducing contamination, but investment in achieving at least comparable depths in the blue (< $1.5\mu\text{m}$) as achieved in the red is also found to be key to fully reducing contamination from high- z samples.

Key words: galaxies: abundances – galaxies: distances and redshifts – galaxies: high-redshift – galaxies: photometry

1 INTRODUCTION

In the first few years since the successful commissioning of the James Webb Space Telescope (JWST), the study of the first billion years of the Universe’s history has undergone a revolution. Exquisitely deep, high resolution imaging and spectroscopy has resulted in the photometric selection of ~ 1000 ’s of high- z galaxies ($z > 6.5$ e.g. Harikane et al. 2023; Adams et al. 2024; Finkelstein et al. 2024; McLeod et al. 2024; Donnan et al. 2024, D’Silva et al. In Prep) and spectroscopic confirmation of ~ 100 ’s (e.g. Bunker et al. 2024; D’Eugenio et al. 2024; Price et al. 2024; Mascia et al. 2024; Heintz et al. 2024). These observations have revealed higher number densities of UV luminous galaxies than first expected from extrapolated HST observations (Oesch et al. 2018; Harikane et al. 2022), pushed the redshift frontier to $z \sim 14$ (Curtis-Lake et al. 2023; Wang et al. 2023; Carniani et al. 2024) and discovered previously unknown classifications of sources (e.g. little red dots Labbé et al. 2023; Matthee et al. 2023; Kokorev et al. 2024).

However, even though JWST provides substantially more information on the Universe than we previously had, there have been cases

where robust looking sources at very high redshifts have turned out to be sample contaminants at lower redshift (Arrabal Haro et al. 2023). Degeneracies between the Lyman and Balmer breaks in a galaxy’s spectra and the chance alignment of strong emission lines, in particular, can result in cases where low- z galaxies enter photometric samples of high- z galaxies (See also discussion in Zavala et al. 2023; Gandolfi et al. 2025, for dusty sources). While spectroscopy is the most powerful tool to obtain precise and accurate redshift measurements, JWST has begun to produce deep fields exceeding AB magnitudes of 30 in depth. In this faint regime, follow-up spectroscopy becomes increasingly time consuming, bordering infeasible in fact due to the anticipated costs to obtain required signal-to-noise ratios (Giardino et al. 2022). The use of medium-width photometric bands, while not producing the level of detail as spectroscopy, may provide a route to increase the confidence of high redshift solutions for ultra-faint sources with smaller overall costs. In Cycle 2, the accepted General Observer programme PID 3215 (PI: D. Eisenstein Eisenstein et al. 2023b) produced ultra-deep imaging in multiple medium width bands over a region the GOODS-South field now dubbed the JADES Origins Field (JOF), reaching AB magnitudes of 30.3 in broad- and medium-width bands (0.32as diameter apertures), providing a total

* E-mail: nathan.adams@manchester.ac.uk

of 14 NIRCcam bands compared to the more standard 7-8 that many other Cycle 1 and 2 programmes utilised.

In the lead up to the launch of JWST, several studies assessed what systematics may plague the selection of high redshift galaxies and quantified what completeness and purities would be expected from hypothetical survey designs (e.g. [Kauffmann et al. 2020](#); [Hainline et al. 2020](#)). With both extreme depths and a wide range of photometric bands, the completed JADES Origins Field provides an opportunity to expand upon this early work given what we now know about JWST data and the initial work studying the early Universe using it. In this study, we explore the impacts that medium-band photometry has on the sample completeness and contamination rates when selecting galaxies at $z > 7.5$.

From this we can also assess the potential impact that the use of medium-bands has on measuring the galaxy UV luminosity function, particularly at the faint-end where completeness and contamination rates vary the most. To accomplish this, we conduct two experiments. The first, we conduct a photo- z selection procedure on the JADES Origins Field using different combinations of the photometric bands available to more closely recreate other survey designs. We then repeat this procedure on images which are intentionally degraded with additional noise levels and assess how completeness and contamination behave given our prior knowledge of the original, multi-band, deep imaging. In parallel, we utilise the JAGUAR semi-analytic simulation and its photometric catalogues ([Williams et al. 2018](#)) to explore if observed trends can be replicated and to trial a few hypothetical scenarios to inform future survey design. We also examine the UV luminosity function for this field and how the different filter sets gives us different realisations of the LF.

This paper is structured as follows: in Section 2 we describe the data and reduction processes used, including the development of custom templates for ‘wisp’ artefacts between 1.5-2.1 microns; In Section 3, we describe the photo- z and SED fitting processes used in this work and conduct an initial analysis of the JOF field; In Section 4 we repeat the analysis from Section 3 using different combinations of photometric bands in combination with simulated catalogues to assess how completeness and contamination may be affected; In Section 5 we intentionally degrade the quality of the JOF imaging and repeat the analysis again to observe how selections behave in the low SNR regime; In Section 6 we discuss our findings in the context of the faint-end of the UV Luminosity Function before summarising our conclusions in Section 7.

2 DATA

This work focuses on the region dubbed the JADES Origins Field (JOF [Eisenstein et al. 2023b](#)). This is a single NIRCcam pointing sub-region of the GOODS South field which has some of the deepest NIRCcam data available from Cycles 1 and 2. In Cycle 1, the field was visited as a parallel to JADES NIRSpec observations of the Hubble Ultra Deep Field (PID 1210, PI: N. Luetzgendorf [Eisenstein et al. 2023c](#)). In Cycle 2, a large programme (PID 3215, PI: D. Eisenstein) was awarded time to revisit this small patch of sky to add in complementary medium bands to comparable depths to the wide bands already available. This field is not only one of the deepest fields currently available, but also contains some of the widest variety of JWST imaging filters available with a total of 14 available (See also the JEMS [Williams et al. \(2023\)](#), Technicolour and MegaScience programmes [Suess et al. \(2024\)](#)).

There is additional data available in this field through the shallower tiers of the wider JADES observing programme in the GOODS-S

Table 1. Average 5σ depths calculated in 0.32 and 0.2 arcsecond diameter apertures for the combined PID 1210 and 3125 data sets. Quoted values are rounded to nearest 0.05 increment and represent the confidence on the raw measured value, not an aperture corrected value.

Filter	Depth (0.32as)	Depth (0.2as)
F090W	29.80	30.75
F115W	29.85	30.85
F150W	30.10	31.10
F162M	29.90	30.90
F182M	30.30	31.25
F200W	30.10	31.05
F210M	30.10	31.05
F250M	29.85	30.65
F277W	30.35	31.20
F300M	30.05	30.95
F335M	30.20	31.00
F356W	30.35	31.15
F410M	29.80	30.50
F444W	30.25	30.95

field. However, these data that are currently public do not uniformly cover the footprint of the JOF, and so we omit them on account of providing only marginal depth improvements at the loss of uniformity, which could complicate the experiments conducted in this work.

We process these images using an adapted version of the official STScI pipeline employed in [Adams et al. \(2024\)](#); [Conselice et al. \(2024\)](#); [Harvey et al. \(2025\)](#). We use version 1.8.2 of the JWST pipeline with CRDS pmap1084. Between stage 2 and stage 3 of the JWST pipeline, we implement our own custom 2D background subtractions on each of the individual calibrated frames before mosaicing. We also implement the subtraction of our own wisp templates (see subsection 2.1). Within Stage 3 of the pipeline, we align our images to the JADES DR2 catalogs ([Eisenstein et al. 2023c](#)) which are in-turn aligned to GAIADR3 ([Gaia Collaboration et al. 2023](#)). After the mosaic is constructed, we conduct a second round of background subtractions, align all of our images to the F277W filter to ensure WCS consistency and finally pixel match the images.

It should be noted that at this stage, the medium band filters F182M and F210M were found to have significant WCS distortion relative to the other bandpasses, particularly in NIRCcam module A. This resulted in offsets upwards of 3 pixels towards detector edges, considering the small aperture sizes used in the source extraction of high- z candidates, such offsets can lead to significant errors in flux measurements. This distortion effect was also noted in the work of [Robertson et al. \(2024\)](#) and corrected by replacing the distortion map with the nearest broadband filter F200W. In February of 2024, calibration pmap1197 was released which implements a formal correction to the problem, we subsequently remade the medium-band mosaics from PID 3215 using pmap1210 (post-correction). We find these new images are greatly improved, with the gradients in our estimated residual distortion removed and with a mean WCS offset of less than 0.8 pixels between photometric bands.

Each source in our catalogue is prescribed a local depth in each photometric band. These are calculated using the normalised median absolute deviation (NMAD) of the nearest 200 empty circular apertures of the same size which are randomly positioned in ‘empty’ regions of the image (defined as being 1 arcsec away from occupied pixels in the segmentation map). We show the mean average depth for the full JOF field in Table 1. These local depths are used in the calculation of the photometric errors and significance of detection for each individual source.

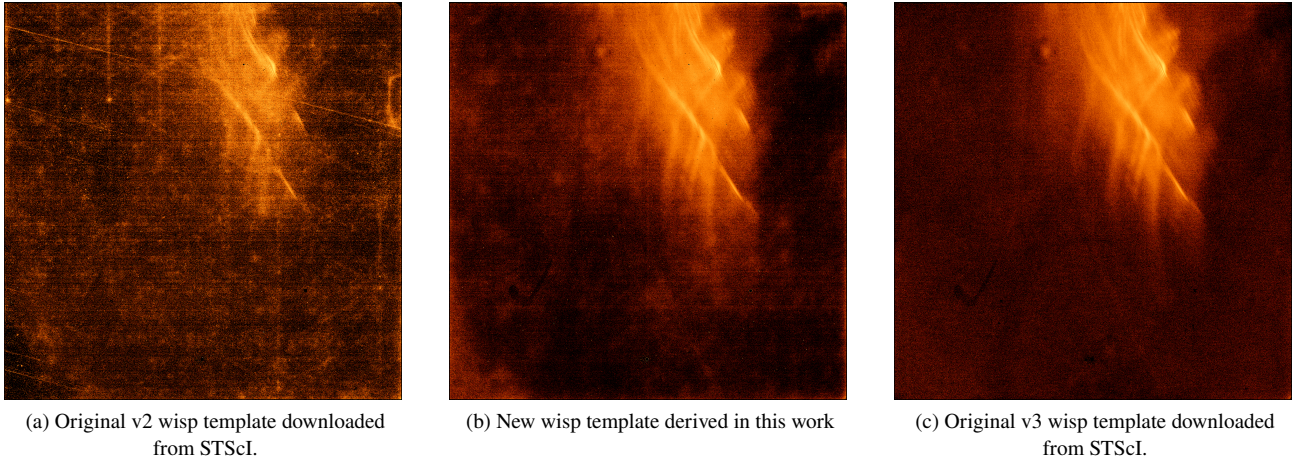


Figure 1. A comparison between NIRCam F150W, b4 module wisp models, with normalisation in the intensity scaling applied to match an aperture placed around the most intense region. Panel a) shows the original wisp template released by STScI in November 2022, panel b) shows the new wisp template developed as part of this work, panel c) shows the latest wisp template model (v3) produced by STScI in Summer 2024. We note that our template closely resembles the newest official template, with the primary difference being that our template has some large scale features in the background which are likely the consequence of the use of slightly older calibrations.

2.1 New Wisp Templates

The NIRCam instrument on JWST exhibits an artefact related to stray light which has been dubbed ‘Wisps’. These artefacts primarily impact the central 4 blue imaging chips (A3, A4, B3, B4) between 1.5-2.1 microns. The precise shape and intensity of these artefacts has some minor wavelength and position dependence, though many studies so far have utilised the subtraction of an intensity-scaled template to remove the majority of this rogue light (see [Robotham et al. \(2023\)](#) for an example of a non-template based methodology). To best correct for this artefact (and any other consistent flat fielding features) in our imaging, we produce our own wisp templates using images produced with the same pipeline and calibration version.

Our own templates are created by conducting a median stack of all STAGE 2 products from a wide selection of deep-field observations. The full list of JWST programme ID’s used are as follows: 1180 (JADES, PI: D. Eisenstein [Eisenstein et al. 2023a](#); [Bunker et al. 2024](#); [Rieke et al. 2023](#); [Eisenstein et al. 2023c](#); [Hainline et al. 2024](#)), 1208 (CANUCS, PI: C. Willott; [Willott et al. 2024](#)), 1210 (JADES, PI: N. Luetzgendorf), 1324 (GLASS, PI: T. Treu; [Treu et al. 2022](#); [Mascia et al. 2024](#)), 1345 (CEERS, PI: S. Finkelstein; [Bagley et al. 2023](#); [Finkelstein et al. 2024](#)), 1895 (FRESCO, PI: P. Oesch; [Oesch et al. 2023](#)), 1963 (JEMS, PI: C. Williams; [Williams et al. 2023](#)), 2079 (NGDEEP, PI: S. Finkelstein; [Bagley et al. 2024](#)), 2738 (PEARLS, PI: R. Windhorst; [Windhorst et al. 2023](#)), 3215 (JOF, PI: D. Eisenstein; [Eisenstein et al. 2023b](#); [Robertson et al. 2024](#)), 4111 (MegaScience, PI: K. Suess; [Suess et al. 2024](#)). This dataset provides around 200 individual ‘_cal.fits’ frames for each NIRCam module over a range of RA and DEC values for the F150W, F200W, F182M and F210M filters. We use Stage 2 outputs in our procedure to ensure our wisps do not duplicate the application of other calibration steps within the pipeline. We switch off the pipeline’s own background subtraction step and replace it with a uniform background subtraction to prevent any pre-subtraction of the wisp artefact by a 2D background model.

Unfortunately the F162M filter is used much less frequently than the F182M and F210M in current observational data of deep fields, resulting in a lower quality template relative to the other bands (average over 50 frames instead of ~ 200 frames). The usage of the band is also dominated by the JADES Origins Field which utilises a small

dithering pattern. To reduce the impact this has on the median stack, we only use six F162M frames from the JOF field in order to prevent significant residuals of real sources (bright galaxies and stars) entering the template. Since the central wavelength is relatively close to the F150W filter, we experiment with reducing the F162M images using our derived medium band template and the F150W template to determine which has the best performance. We find the F150W template produces the lowest average background level for the final F162M mosaic but leaves small regions over or under subtracted where the wavelength dependence has spatially shifted some of the highest intensity wisp features. Since the unique depth of the JADES Origins Field is its primary selling point, we opt for the low background produced by the F150W template in exchange for masking a small amount of improperly handled artefact.

Before subtraction of the wisp from our calibrated images, we first place circular apertures in a grid around the image and the template in order to estimate a scaling factor to be applied to the template before subtraction. We calculate this scaling factor using the brightest 10 per cent of apertures when placed on the wisp template (the most affected regions) for each of the NIRCam modules. Following testing with Epoch 1 of the NGDEEP field (PID: 2079 PI: S. Finkelstein), we find that corrected modules now have the same average depth as those which are unaffected by wisps (A1, A2, B1, B2) within 0.04 magnitudes. Confident this procedure works, we apply our templates to the JADES Origins Field. We find that our templates are also effective here, with the average depth of wisp affected modules within 0.02-0.10 magnitudes of the non-affected modules, with the greatest difference being with the deepest medium band of F182M.

We show an example of our wisp template in F150W module B4 within Figure 1. We show this alongside the V2 (Nov 2022) and V3 (Summer 2024) wisp templates produced by STScI ¹. We find our template has a significantly lower background compared to the V2 template, has removed features consistent with residuals of real sources in the median stack (e.g. stellar diffraction spikes) and reveals

¹ <https://jwst-docs.stsci.edu/known-issues-with-jwst-data/nircam-known-issues/nircam-scattered-light-artifacts#NIRCamScatteredLightArtifacts-wispsWisps&gsc.tab=0>

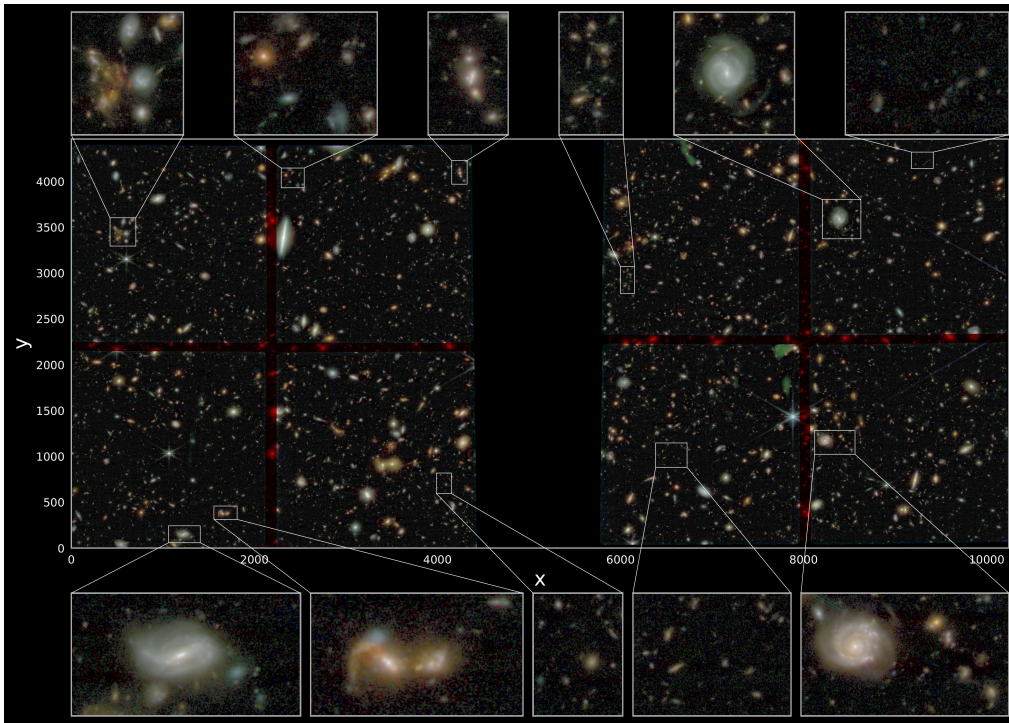


Figure 2. A tour of an RGB image of the JOF field. The image was generated using the *trilogy* package (Coe et al. 2012) with the broadband images of the field. Bright, green regions in the NIRCcam b4 module (lower left of the right side module) indicate masking of residual wisp artefacts. The red, cross-shaped pattern in each side of the image (caused by the blue module gaps) are similarly masked in our analysis.

the wisp artefact to be more extended. The shape and intensity of the artefact is very similar to that of STScI’s V3 template, though our template exhibits larger scale features in the background which may be a consequence of residual flat fielding due to our usage of the older *pmmap* versions. Since we know our template was constructed using the same pipeline and calibration versions as our science images, we proceed with the use of this template. The final RGB mosaic is presented in Figure 2.

3 GALAXY SELECTION PROCEDURES

A catalogue of the sources in the Jades Origins Field is produced using the *SExtractor* software in dual image mode. Here, a weighted stack of the red broad band images (F277W, F356W, F444W) is used at the selection band. Aperture photometry is measured in both 0.2 and 0.32 arcsecond apertures. A set of science images PSF homogenised to the F444W band are also produced using empirical PSF models generated following the technique used in Weaver et al. (2024). We find the profile of the PSF model is similar in shape but slightly broader than theoretical models generated by *WebbPSF* (Perrin et al. 2012, 2014). In the following subsections we describe how we select and measure the galaxies using different criteria and later how the results depend on these.

3.1 Photometry and Photo-Z procedure

Photometric redshifts for our sources are conducted with the use of the *EAZY*-py SED fitting tool (Brammer et al. 2008). Here, we employ the use of the default *FSPS* templates as well as Sets 1 and 4 generated in the work by (Larson et al. 2023). These additional templates provide galaxy spectra which are younger, bluer and have

stronger emission lines compared to the default template set on its own. *EAZY* is run using the Madau (1995) treatment for absorption by neutral Hydrogen, adds dust attenuation up to 3.5 magnitudes from Calzetti et al. (2000) and employs no galaxy luminosity prior. *EAZY* is run twice with upper redshift limits of 25 and 6 in order to conduct a direct comparison between the best fitting high-*z* and low-*z* solutions. We also investigate how our results would change when using different size apertures.

To assess our photometric redshifts, we compare our outputs to 20 spectroscopic redshifts crossmatched from ‘v3’ of the Dawn JWST Archive (DJA: Heintz et al. 2024). All 20 sources originate from PID 2198 (PI: L. Barruffet Barruffet et al. 2024) and are luminous sources $23 < m_{F277W} < 26$ between redshifts $1.2 < z < 5.4$ with the majority of targets between $3 < z < 4.5$ (See Figure 3). We find that 19/20 sources have redshifts consistent with their spectroscopic results. The one outlier has spectroscopic redshift of $z = 4.4358$ and an uncertain photometric redshift of $z = 5.9^{+0.0}_{-3.8}$ featuring 3 strong peaks in its probability density function at $z = 5.9, 4.2$ and 2.1 . More spectra of this sub-field was taken as part of the JADES programme (under PID 1287, PI: K. Isaak) in January 2024. We have reduced the PRISM spectra from this programme following the default *NIRSpec* settings of the *msaexp* tool¹, which is similar to the methods used by the DJA. For our purposes we only show 13 conservative spec-*z* results with 2 or more emission lines identified with by-eye vetting. We also include a compilation of historic spectroscopic redshifts from Merlin et al. (2021), which features 122 cross-matches with 3D-HST (Momcheva et al. 2016), ACES (Cooper et al. 2012), (Morris et al. 2015), Ravikumar et al. (2007), Szokoly et al. (2004), VANDELS (Garilli et al. 2021), Balestra et al. (2010), VUDS (Le Fèvre et al.

¹ <https://zenodo.org/records/7579050>

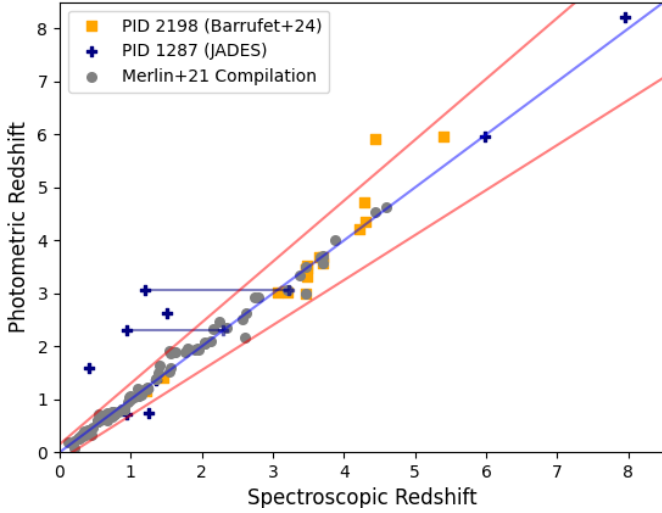


Figure 3. A comparison of our photometric redshifts using the full JOF dataset against publicly available NIRSpc programmes covering the JOF field (Barrufet et al. 2024; Carniani et al. 2024) and historical spectroscopic redshifts in the Merlin et al. (2021) compilation. Two JADES PRISM spectra obtain bimodal spec- z solutions which we indicate with a connecting line showing the photo- z prefers one solution over the other.

2015), VVDS (LeFèvre et al. 2013) and Vanzella et al. (2008). A visual comparison is shown in Figure 3.

3.2 High- z Selection Criteria

High redshift galaxies at $z > 7.5$ are selected following the criteria and are similar to those used in the construction of the EPOCHS sample (Adams et al. 2024; Conselice et al. 2024; Austin et al. 2024). We summarise the primary cuts below:

(i) $\leq 3\sigma$ detections in all bands blueward of the expected Lyman break.

(ii) $\geq 5\sigma$ detection in the first 2 bands directly redward of the Lyman break, and $\geq 2\sigma$ detection in all other redward bands, excluding medium bands. If the galaxy appears only in the long wavelength NIRCcam photometry (i.e. a F200W or higher dropout), we increase the requirement to a 7σ detection to minimise the potential for selecting red camera artefacts which can appear to look like noisy $16 < z < 18$ sources.

(iii) $\int_{0.90 \times z_{phot}}^{1.10 \times z_{phot}} P(z) dz \geq 0.6$ to ensure the majority of the redshift PDF is located within the primary peak.

(iv) $\chi^2_{red} < 3(6)$ for best-fitting SED to be classed as robust (good).

(v) $\delta\chi^2 \geq 4$ between high- z and low- z EAZY runs (where maximum redshift is set to 6). This ensures that the high- z solution is much more statistically probable.

(vi) If the 50% encircled flux radius (FLUX_RADIUS parameter in SExtractor) is consistent with the size of the PSF in the F444W band, then we require that $\delta\chi^2 \geq 4$ between the best-fitting high- z galaxy solution and the best-fitting brown dwarf template (Marley et al. 2021; Harvey et al. 2025) which can look like high- z galaxies (Holwerda et al. 2024).

(vii) 50% encircled flux radius is ≥ 1.5 pixels in the long-wavelength wideband NIRCcam photometry (F277W, F356W, F444W). This avoids detecting hot pixels in the LW detectors as F200W dropouts.

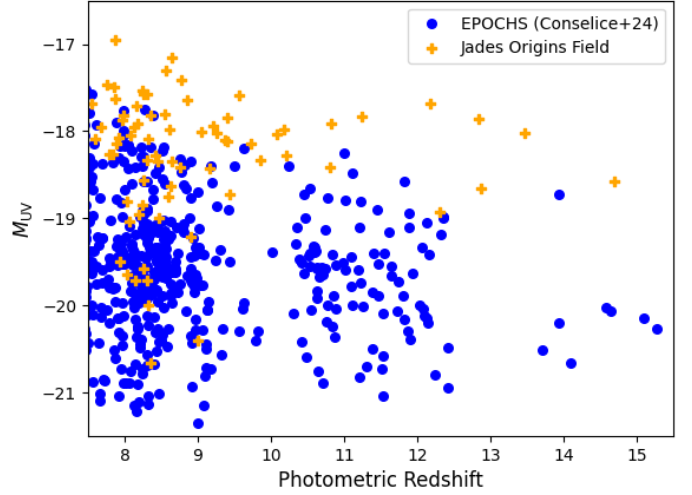


Figure 4. A comparison of the redshifts and M_{UV} values obtained for the full JOF sample vs the EPOCHS sample (Conselice et al. 2024) which compiled a number of wider area, but shallower surveys together. Here, we see the JOF field enables intrinsically fainter sources to be identified.

3.3 The initial full sample of high- z candidates

Utilising the full set of NIRCcam data available in this field and conducting the above photo- z selection procedure, we obtain 50 galaxies which we class as robust at $z > 7.5$ using the full JOF dataset. The distribution of sources is as follows, with a full table of high- z candidates presented in Table A1: 27 sources with $7.5 < z < 8.5$, 12 sources with $8.5 < z < 9.5$, 7 sources with $9.5 < z < 11.5$, 2 sources with $11.5 < z < 13.5$ and 1 source with $z > 13.5$. Redshifts and M_{UV} values for the sample are shown in Figure 4. Since we only utilise JWST data in our selections, our sample is incomplete at $z < 8.0$ due to the demand for a complete break to be observed and the lack of data bluewards of 0.9 microns. While HST data is present in this field, it is significantly shallower (mag 28.3–29.1 in F606W) and non-uniform (Whitaker et al. 2019). Since ultra-deep HST data can not always be a guarantee for such JWST fields, we focus on the use of just JWST photometry for the purpose of this study. Below we discuss some of the details of our selected galaxies and comparisons to previous similar studies on this field.

3.3.1 A robust candidate galaxy at $z \sim 14.7$

The highest redshift, robust galaxy in our catalogues that passes visual inspection is a faint ($m_{AB} \sim 29.8 - 30$) galaxy which is selected at $z = 14.6 - 14.9$ (See Figure 5) with a $\delta\chi$ of 15 relative to a low redshift solution at $z = 4.2$. This agrees with the $\delta\chi^2$ expectations set out in the JOF survey paper (Eisenstein et al. 2023b). Key for determining this is the slightly blue slope measured in the detected bands and the lack of line emission in the F250M band, which covers H β and O[III] at $z = 4.2$. This object is also identified in Robertson et al. (2024) as their highest redshift robust candidate with $z = 14.6$, meaning this source has now been selected as robust with very similar photometric redshifts in two completely independent works. NIRSpc spectroscopy was taken of this source, but due its faint luminosity and the large slit losses in the observations, no definitive redshift was obtained (Carniani et al. 2024).

Table 2. The 15 high- z galaxy candidates in the JADES Origins Field presented in [Robertson et al. \(2024\)](#). We split the sources by their original classification as Robust ($z > 11.5$), Contributing (some $P(z) > 11.5$) and Secondary ($z > 11.5$ but failing some selection criteria). Alongside the original JADES teams findings, we present our equivalent photometric redshift estimations and classifications. ‘Faint’ describes sources that are $< 5\sigma$ detected in the first two bands redwards of the Lyman Break. Our use of 0.32as apertures does mean the faintest sources are lost for this reason. ‘Blended’ sources are flagged as potentially having rogue light from a close neighbour within the aperture. ‘Masked’ sources are typically near module edges or stellar diffraction spikes. Objects with ... values did not obtain a successful SED fit.

Name / Coordinates	JADES Class	JADES z	Our z (0.32as)	Our z (0.2as)	EPOCHS Comments
JADES+53.09731-27.84714	Robust	11.53	$9.0^{+1.5}_{-0.35}$	$9.2^{+1.5}_{-0.2}$	Faint, Broad PDF
JADES+53.02618-27.88716	Robust	11.56	$11.4^{+0.3}_{-0.4}$	$11.4^{+0.3}_{-0.2}$	Robust
JADES+53.04017-27.87603	Robust	12.10	$11.3^{+0.4}_{-0.3}$	$11.9^{+0.1}_{-0.7}$	Faint
JADES+53.03547-27.90037	Robust	12.38	$16.3^{+0.35}_{-0.4}$	$14.5^{+0.5}_{-0.4}$	Faint
JADES+53.06475-27.89024	Robust	12.93	$12.9^{+0.2}_{-0.1}$	$12.9^{+0.1}_{-0.1}$	Robust
JADES+53.02868-27.89301	Robust	13.52	$12.3^{+0.3}_{-0.2}$	$12.3^{+0.1}_{-0.1}$	Robust
JADES+53.07557-27.87268	Robust	14.38	$16.9^{+0.2}_{-0.5}$	$16.5^{+0.3}_{-0.1}$	Faint
JADES+53.08294-27.85563	Robust	14.39	$3.6^{+0.1}_{-0.1}$	$3.7^{+0.1}_{-0.1}$	Balmer Break, Blended, (Spec- z 14.32)
JADES+53.10762-27.86013	Robust	14.63	$14.9^{+0.8}_{-0.3}$	$14.6^{+0.2}_{-0.2}$	Robust
JADES+53.07248-27.85535	Contributors	10.61	$11.9^{+0.1}_{-0.6}$	$11.3^{+0.2}_{-0.3}$	Faint (0.32), Robust (0.2)
JADES+53.03139-27.87219	Contributors	10.76	$11.0^{+0.4}_{-0.6}$...	Faint
JADES+53.09292-27.84607	Contributors	11.05	$0.2^{+8.2}_{-0.1}$	$0.0^{+10.2}_{-0.0}$	Faint, low- z 1.6 micron bump, Masked
JADES+53.06857-27.85093	Contributors	11.17	Blended, Masked
JADES+53.08468-27.86666	Secondary	12.90	$3.5^{+10.4}_{-0.2}$	$12.8^{+0.9}_{-0.2}$	Balmer Break (0.32), Robust (0.2)
JADES+53.07385-27.86072	Secondary	13.06	$1.7^{+6.3}_{-0.45}$	$1.6^{+1.1}_{-0.6}$	Balmer Break

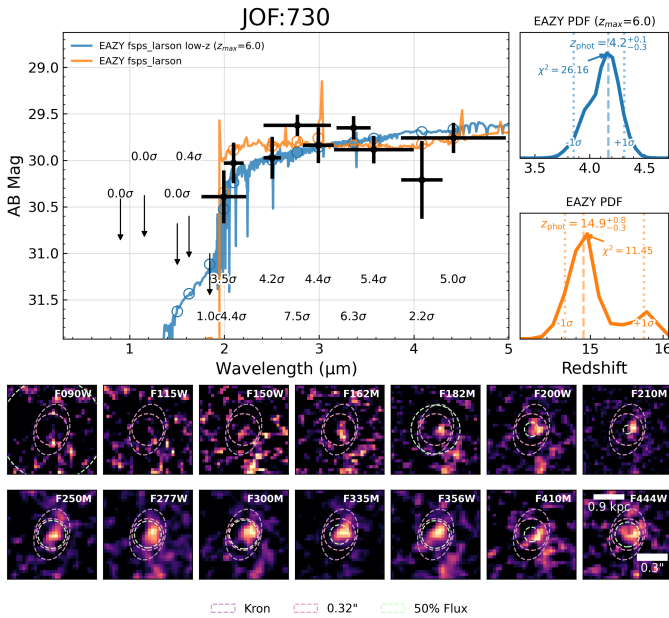


Figure 5. The SED fit for JADES+53.10762-27.86013 (known as JOF:730 in the our catalogues), the highest redshift robust candidate. Displayed are the EAZY fits for the high- z solution in orange, low- z solution in blue.

3.4 Comparisons to the sample selected in Robertson+24

The official JOF team released their initial sample of high- z galaxies in [Robertson et al. \(2024\)](#). This consisted of nine robust galaxies at $z > 11.5$, including four robust galaxies with redshift PDF’s extending above $z > 11.5$ and a further two less confident galaxies at $z > 11.5$. We find cross matches to all 15 objects in our catalogues with typical matching separations less than a pixel. Only 4 of these 15 galaxies enter our robust sample. The primary reason for non-selections are that these galaxies fall just below our 5σ selection criteria, this is because we initially utilise 0.32 arcsecond diameter apertures while [Robertson et al. \(2024\)](#) uses 0.2 arcsecond diameter apertures. As a result, their faintest sources are typically 3-4 σ

detected in our work, though we find the majority still have high- z primary solutions.

For a full breakdown of our findings for the sources presented in [Robertson et al. \(2024\)](#), we find that: 4/9 sources in their main sample are selected in our work, 0/4 of their lower redshift sources are selected and 0/2 of their dubious sources are selected. In total, four sources are identified in our work to be at $z < 4$ and better fit by Balmer breaks than Lyman-breaks. These include both of the sources described as dubious in the work by [Robertson et al. \(2024\)](#). The additional two include one of their lower- z candidates and the, now spectroscopically confirmed, $z = 14.32$ source which is blended with a $z = 3$ neighbour resulting in 3σ detections in the bluest bands. We find one source is better fit at $z \sim 9$ as opposed to $z \sim 11$, however this source has a redshift PDF with a large positive wing and so it is not in significant large tension with the initial [Robertson et al. \(2024\)](#) estimations.

3.5 Differences when using 0.32 or 0.2 arcsecond apertures

Various studies targeting high redshift samples have primarily made use of two different sized circular apertures when conducting initial flux measurements. These have been 0.3-0.32 arcsecond diameters (amounting to 5-6 pixels in radius) or 0.2 arcsecond diameters (amounting to 3.3 pixels in radius). There are potential advantages and disadvantages to using each. The use of larger apertures is slightly more forgiving for the precision of the WCS alignment between photometric bands and it encloses more flux from the PSF ($\sim 70 - 80\%$), requiring smaller aperture corrections. The smaller aperture size can enable higher SNR measurements to be made but can be more greatly influenced by bad pixels, correlated noise, minor image misalignments and it requires larger corrections for flux outside of the apertures. At a radius of 0.1as, the PSF for JWST’s reddest bands has a very steep slope for its encircled flux verses radius, meaning precise PSF models are required as small changes to the FWHM will result in larger changes in the aperture correction verses the use of a larger aperture.

To assess if there are significant differences in sample selection as a consequence of this choice, we repeat our selection procedure on a catalogue using 0.2 arcsecond apertures. This catalogue selects

76 sources at $z > 7.5$ compared to the 50 sources that the 0.32as catalogue did. Of these sources, 46 are consistent between the two samples. The primary reason sources are lost are due to the poorer χ^2 of the fit, with only one source gaining a significant detection in blue bands when smaller apertures are used. This source was at $z = 8$ and in the regime where pure JWST selections become incomplete due to the positioning of the Lyman break within the F090W band. Of the 30 sources gained, 50% (15/30) were below the 5σ regime of the 0.32 arcsecond catalogue and 30% (9/30) were in the $5-7\sigma$ regime in the previous 0.32 arcsecond catalogue. Under the assumption these redshifts are correct, this amounts to a $\sim 40\%$ completeness in the $5-7\sigma$ regime in this field when using 0.32as apertures. This completeness is lower than anticipated from our simulation work which we conduct in Section 4.2, however it is dependent on a very small number of sources. We conduct more comparisons between these catalogues in later sections, such as seeing if they produce a consistent UV Luminosity Function. Additional objects selected with the 0.2as aperture catalogue are also included in Appendix A alongside our fiducial catalogue.

Among the faint sources added to the high- z sample are an additional two galaxies from the Robertson et al. (2024) sample. Non-selected galaxies from that work with high- z solutions typically only just fail our detection criteria (e.g. 4.5σ in rest-frame UV). The spectroscopically confirmed galaxy at $z = 14.32$ remains non-selected even with the smaller aperture size on account of contamination from the neighbouring source producing a 2.4σ flux in F115W.

The use of smaller apertures also reveals three new ultra-high redshift sources at $z > 15$ in our selections. One at $z \sim 22$ is immediately rejected by eye as likely being a shredded segment of a larger resolved source. The source labelled as ID 7891 ($z = 15.9$) in Appendix A has dubious F300M and F444W fluxes which draws suspicion over whether the source is a Balmer break at $z \sim 4.2$ with $H\beta/O[III]$ and $H\alpha$ impacting band measurements around 2.5 and 3.5 microns respectively, as F300M and F444W indicate a lower potential continuum level than fit. The source labelled as ID 908 ($z = 17.3$) has $< 5\sigma$ detections in 4/7 of the bands it is detected in and $< 3\sigma$ detections in 3/7 bands, making its precise SED shape relatively uncertain, particularly redwards of 4 microns. Consequently, the $z \sim 14.6 - 14.9$ source presented in Figure 5 remains the most robust looking ultra-high- z source in the sample and it is selected with both choices of aperture size. With the smaller aperture size, the $\delta\chi^2$ to a low- z solution increases from 15 to 35 for this source.

4 QUANTIFYING THE ADVANTAGES OF MEDIUM BANDS

The JADES origins field is the the only blank field to reach AB magnitude depths of 30+ in such a variety of wide and medium photometric bands. It thus presents a great playground for observing the impacts that such a sampling of galaxy SED's provide. In this section, we explore how the addition of medium-width bands impacts the selection of high redshift candidates. We conduct this study both through the use of real data from the JOF field and with the use of mock catalogues generated by the JAGUAR semi-analytic model (Williams et al. 2018).

4.1 Adding and Removing Bands from Real Data

To begin, we repeat our photometric redshift and selection procedures from Section 3 but with more restricted combinations of photometric bands. These runs are designed to replicate the filter choices of

other JWST deep field observations and so include the use of no medium-width bands (similar to e.g. GLASS & NGDEEP), the use of just F410M (similar to e.g. CEERS & PEARLS) and the use of both F410M and F335M (e.g. JADES). We respectively name these catalogues C-0, C-1 and C-2 to indicate the number of medium-width bands used. Our fiducial catalogue containing the full JOF dataset is named C-ALL. In this section, we examine the changes to the selected high- z sample (both sources which are lost from the fiducial sample and added to the fiducial sample) in order to examine how variable high- z selections can be and what the reasons are for this variability.

Our original selection using the full dataset (C-ALL) identified 50 galaxies at $z > 7.5$. When applying our selections to the three catalogues with fewer medium bands (C-0, C-1, C-2), each respectively identified 46, 51, 51 candidates. Of these objects, 41, 44, 45 objects are consistent with the fiducial sample (C-ALL), showing that sample overlap with C-ALL is relatively high (82-90%) and increases with increasing numbers of photometric bands. The largest increase in sample overlap occurs when a single medium-band is added to the broad-band-only dataset. Sources which are identified as confident in C-ALL but omitted when fewer bands are used are consistent between the different band combinations (e.g. sources selected in C-ALL but omitted in C-2 were also omitted in C-1 and C-0).

We begin our analysis by examining the 9 objects omitted from selection when comparing the C-ALL catalogue to the C-0 catalogue. Half (5) of these sources are low SNR, with F200W detections at $< 8\sigma$. The remaining 4 are between 8σ and 12σ . All objects retain initial high- z solutions in C-0, C-1 and C-2 but they fail χ^2 requirements regarding significant secondary low- z peaks, indicating these sources are lost from the sample due to inadequate confidence regarding the Lyman and Balmer break degeneracy. This degeneracy is reduced when medium-width bands reveal a lack of optical emission lines. One of the sources lost is JADES+53.02868-27.89301 from Robertson et al. (2024), here we find this object is only selected in the C-2 or C-ALL catalogues and not in C-0 or C-1. This both highlights the potential benefits that multiple medium bands can provide high- z selection and also shows that we should not entirely overlook lower confidence sources in other surveys which may be unselected as a consequence of expected incompleteness levels (In this case, a $z \sim 12-13$ candidate could have been overlooked if located in another survey programme).

We next examine sources that are added to the high- z sample when fewer bands are used. For the C-0, C-1 and C-2 catalogues we find that 5, 7, 6 new sources are selected compared to the C-ALL sample. These extra sources are largely consistent between these catalogues, with 3/5 and 6/6 sources in the C-0 and C-2 catalogues appearing in the C-1 catalogue. This means there are 9 unique sources which get selected as high- z when fewer photometric bands are available. We find that the sources that are selected outside of the C-ALL catalogue are faint, with 6/9 sources below 8σ in the rest frame UV. When examining these new sources in the C-ALL catalogue, we find 2/9 sources have primary photo- z solutions that are low- z Balmer breaks whilst all others have similar high- z primary solutions but do not meet $\delta\chi^2$ cuts relative to low- z solutions. Overall, the inclusion of many medium-width bands reveals that these faint sources are more uncertain than first thought with the sole use of wide bands.

There are two out of the nine sources that are not selected in the C-ALL catalogue which are potentially legitimate high- z sources. One source (the brightest one) is a legitimate looking $z = 7.4$ candidate which scatters above our $z > 7.5$ selection only in C-0. The second source may be potentially legitimate but faint. Its photometric redshift of $z = 10.2$ places it on the boundary where the Lyman break is just

entering the F150W bandpass. Between the different catalogues, this object sometimes used the F150W and F200W or F200W and F277W bands for the 5σ detection cuts and its F277W detection was 4.95σ . So there were instances where if the primary redshift solution was slightly high it was not selected on account of being too faint. Due to its faintness, this source lies within the expected low completeness regime (explored in the next subsection).

In brief, sources that are selected as robust, high- z galaxies in one combination of photometric bands, but not in another, tend to be faint and largely maintain a primary high- z solution in all catalogues. The key difference that impacts their ‘robust’ classification is the relative confidence of the high- z solution compared to the next-best-fitting low- z solution, where the addition of medium bands can either increase or decrease this confidence relative to a broad-band-only catalogue.

4.2 Results when repeating the experiment on a simulated catalogue

To contextualise the results from observations, we employ the use of the JAGUAR semi-analytic model and the mock photometry that was generated from it (Williams et al. 2018). This particular SAM was used due to its performance in replicating galaxy colours in JWST photometric bands (Wilkins et al. 2023). We use three different realisations of the JAGUAR simulation to provide over 300 square arcminutes of simulated sky area, a factor of 30 greater than probed by the JADES Origins Field. We use such a large area in order to produce a large statistical sample of high- z galaxies and assess if similar behaviours witnessed in the observations are replicated. The catalogues have a magnitude cut applied 1 magnitude fainter than the 5σ limits of the JOF field. This results in approximately 1 million sources in total across all redshifts.

Multiple simulated catalogues are generated using different combinations of filters as trialled in the previous section. We scatter the photometry of the simulated sources based on the average depths in each photometric band measured for the JOF field. The catalogue is then formatted in the same way as our observed catalogue and the mock observations run through our EAZY pipeline. This process is repeated 5 times for each of the different filter combinations we use to assess the sensitivity of results to the random scatter applied to photometry. We find that completeness and contamination rates scatter by around 4 percentage points between different realisations of our catalogues. To quantify the impact the addition of medium-width photometric filters has in a high- z context, we focus on the completeness of high- z objects selected and the contamination rate of low- z ($z < 6$) sources entering the sample.

We also add in some additional hypothetical situations to explore avenues for further improving photo- z performance. In one run (deep_blue), we increase the depth of the bluest JOF bands (F090W, F115W) by 0.4 mags (equivalent to 2X exposure time) to make their depths more comparable to the rest of the wavelength range (AB mag 30.2). In a second run (all_band) we add in the remaining medium-width bands of F140M, F360M, F430M, F460M and F480M. These are set to have the same depth as their neighbouring medium-width band, so 29.9 for F140M and 29.8 for the red bands.

We present the full result of simulating photometric redshifts in Figure 6. We find that the inclusion of more medium-width bands leads to reductions in outlier rate and scatter. Outlier rate and scatter also increase towards fainter luminosities and a cloud of contaminant low- z galaxies at $z_{\text{true}} \sim 3$ and $z_{\text{phot}} \sim 11$ also increases in density. Adding medium-width bands between 2-3 microns reduces

this cloud, but adding depth to the blue broad-bands is most effective at reducing the number of objects lying in this undesirable region.

Our selection criteria is designed to identify sources at $z > 7.5$, however there are a large number of sources around this boundary which scatter above and below this selection limit as a consequence of the use of photo- z 's. To simplify discussion of completeness and contamination, we consider sources with a true redshift of $z > 8$ in the following subsections. We also break up this discussion into two redshift bins; $8 < z < 10$ and $z > 10$. In the lower redshift bin, the presence of the Balmer break and rest-optical emission lines may result in different behaviours when applying medium-width bands when compared to higher redshifts where the available UV emission lines are typically weaker and photometry generally probes the UV slope. We present the results of this process in Figure 7 and discuss them in more detail in the following subsections.

4.2.1 High- z Sample Completeness

No single selection criteria is entirely perfect when working with noisy data. Inevitably, a balance is struck between completeness and contamination with every effort made to maximise the former and minimise the latter. In this work, we examine the number of true sources at $z > 8$ in the JAGUAR catalogs that are recovered by our selection processes when various combinations of medium-width bands are used.

Beginning with the redshift bin of $8 < z < 10$, we find that completeness (Number of sources at $z > 8$ selected divided by the total number of $z > 8$ sources) is generally high when considering sources at $10\sigma+$. Without any medium-band information, this completeness is over 80% at the 10σ mark, while including even a single medium band can substantially raise this to 90%. As would likely be expected, increasing the number of medium-width bands leads to an increase in completeness, though the largest benefit comes from the inclusion of a single medium-width band and subsequent bands are less impactful. This improvement with a single medium-width band is noted in the previous subsection, where the biggest jump in the JOF sample overlap was when only F410M was added to the catalogues. From a sample completeness perspective, these results thus support the general ‘deep-field’ design of including a single medium-width band and F410M presents one of the better balances of sensitivity and longest wavelength (to study e.g. emissions lines to highest redshifts or the Balmer break up to $z \sim 10$) as has been employed by many early survey designs as a balance of cost versus effectiveness.

Examining higher redshifts at $z > 10$, completeness is very high (97%+) for sources detected to $10\sigma+$, however the number of these sources present in the simulation at these luminosities is very low. As observed for the $8 < z < 10$ sources, completeness turns over and falls off below 10σ . The use of 0, 1, 2, or even 7 medium-width bands does not provide a significant difference in the completeness curve, due to the lack of any strong, defining features present in the rest frame UV. It is only in our hypothetical scenarios that completeness is improved, with either the inclusion of the reddest medium bands or greater depths in the blue broad bands leading to notable improvements in the 5-8 σ regime.

4.2.2 High- z Sample Contamination

Contamination is when members of an unwanted sub-population enter a sample selection. In our case, contaminant galaxies are those which are of significantly lower redshift ($z < 6$) than the target sample of $z > 7.5$. The contaminating fraction is defined as the

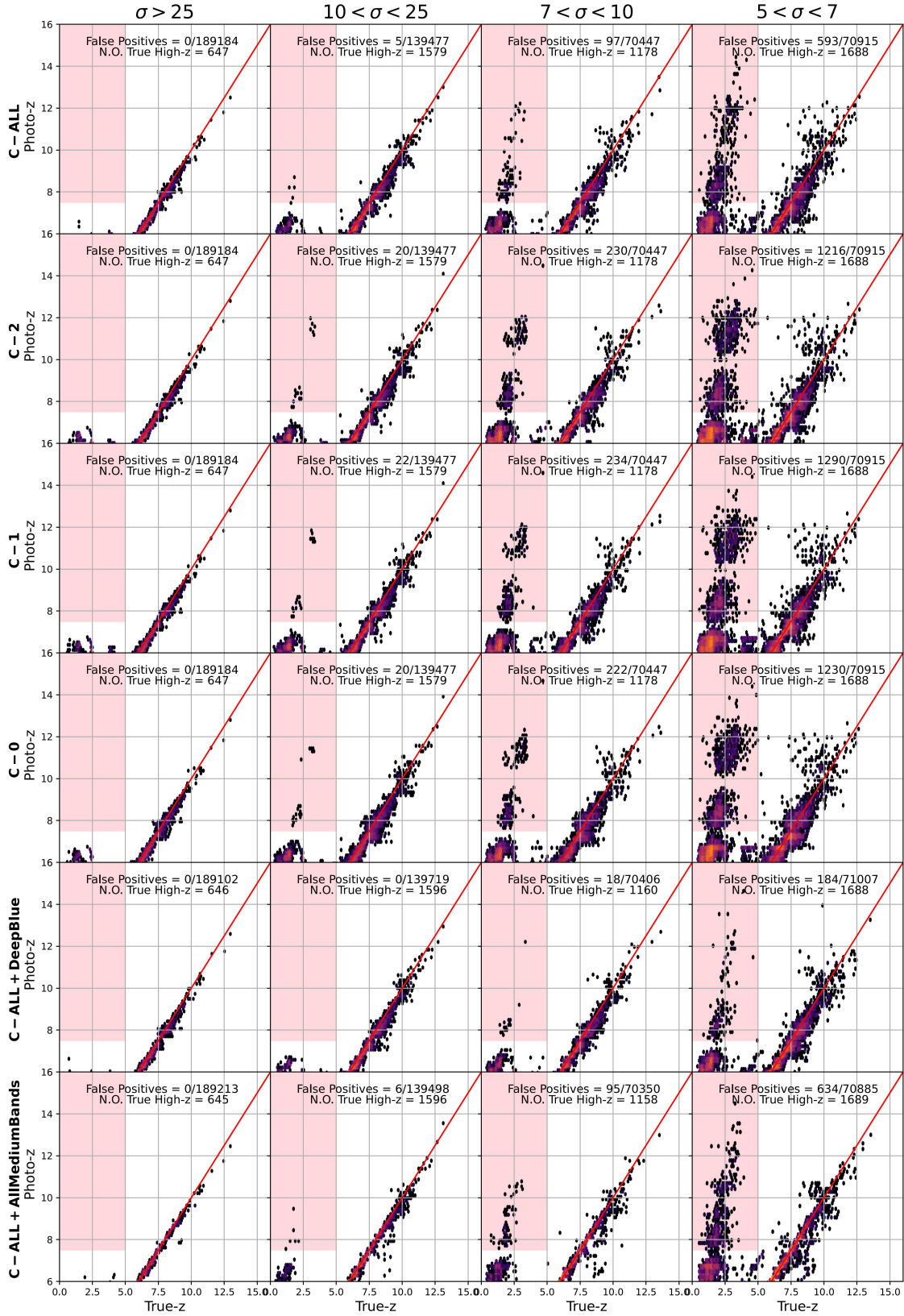
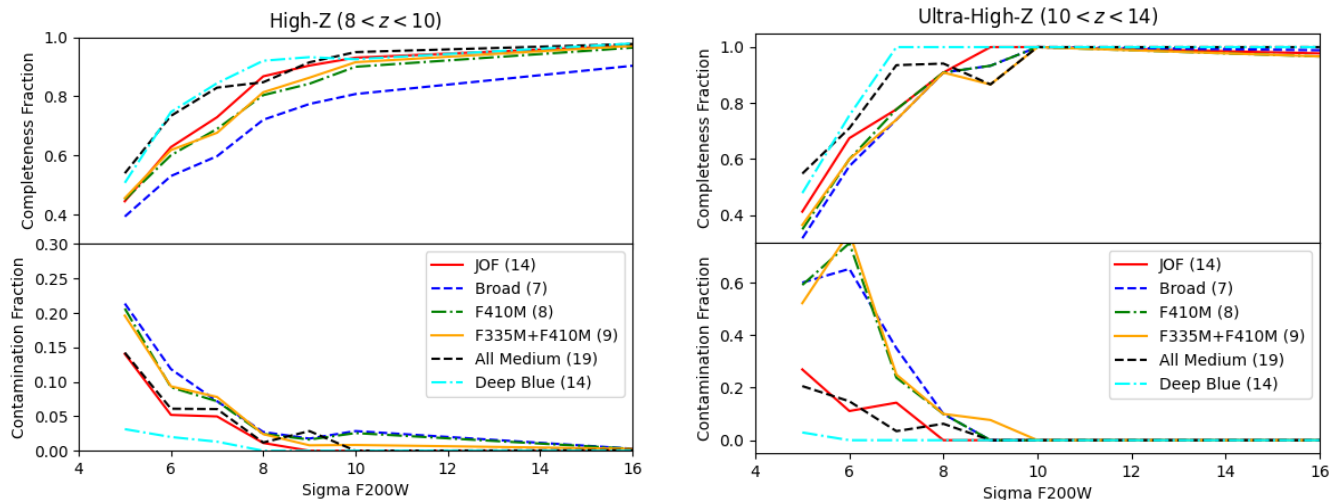


Figure 6. A break down of the photo-z performance on our simulated JAGUAR catalogues. Brighter objects (defined in blocks of sigma confidence in F200W) are grouped to the left and fainter objects grouped to the right. Results for the various filter combinations are shown vertically, with the catalogue name provided on the y-axis label. False positives indicate the number of $z < 5$ galaxies with a fit photo-z greater than 7.5 (shaded region). Brighter objects have greater photo-z performance, in addition, more photometric bands and deeper blue photometry improves outlier rates and scatter. Crucially, the inclusion of the JOFs medium-width bands around 1.5-3 microns greatly decreases the cloud of low-z sources identified at very high-z. Displayed are raw photo-z's, not a final high-z selection which is explored in Figure 7, χ^2 cuts on low-z solutions and other quality cuts greatly reduce the cloud of contaminants. Further improvements would benefit from additional broadband time at 0.9-2 microns to rule out Balmer breaks.



(a) Selection Completeness & Contamination rates for high-redshift sources ($8 < z < 10$) in the JAGUAR simulation

(b) Selection Completeness & Contamination rates for ultra-high-redshift sources ($10 < z < 14$) in the JAGUAR simulation

Figure 7. Completeness and Contamination fractions as measured by running simulated JAGUAR catalogs through our selection pipeline using the observational set up of the Jades Origins Field. The top component of each figure is completeness, while the lower component is contamination. Each line describes the results from one observational set up. The red solid line describes the findings using the fiducial Jades Origins Fields combination of filters and depths achieved within those filters. The blue dotted line shows the results when all medium bands in the JOF field are omitted from use, leaving only broad-width bands. The green dash-dotted line shows results where the F410M medium-band is used in conjunction with broad bands. The solid yellow line further adds the F335M medium band. The final two lines show hypothetical survey expansions to the JOF field, ‘All Medium’ adds all remaining medium-width bands to the JOF field to similar depths while ‘Deep Blue’ doubles the exposure time (0.4 mags) in bands bluer than 1.5 microns. With increasing numbers of medium bands, completeness is observed to increase while contamination decreases. The legend indicates which bands were used and the total number of bands. Lines typically scatter by up to 4 percentage points when repeated 5 times with random elements re-rolled, with larger scatter in the 5–6 σ regime in the ultra-high-z bin.

number of these low- z sources divided by the total number of sources (contaminant plus true) selected. In all of our simulated runs, we find that contamination is generally low for the JADES Origins Field. Even without the use of medium-width bands, contamination is zero for sources detected to $15\sigma+$ and begins to rise at increasing rates as the 5σ level is approached. The primary reason is with such high significance in the detections, the measured depth of the Lyman break discounts the potential Balmer break alternative in the bluer bands.

The inclusion of only 1 or 2 medium-width bands is found to make minimal difference to the total contamination rates, this is because these bands probe narrow wavelength ranges and so there are limited redshift ranges where medium-width bands have the potential to exhibit notably different fluxes (due to the presence of atomic lines) compared to their neighbouring wide- or medium-width bands. With the inclusion of a diverse range of medium-width bands, such as the 7 total medium bands used in the JOF fields, there is a notable reduction in contamination rates. Crucially, the Jades Origins Field employs the use of generally bluer medium-width bands (1.6–3.35 μm) which probe the potential locations of rest-frame Balmer and Oxygen emission lines for the low- z Balmer break contaminants.

Contaminant galaxies are typically misidentified Balmer break sources at $1.5 < z < 4.5$. These misidentifications are driven by shallower bands probing the break regime (F090W and F115W, which are 0.3–0.5 mags shallower than the other broad-width bands) and the convenient positioning of strong emission lines within the broadband filters can replicate a blue SED slope of a high- z galaxy. Within Figure 8 we display two examples of low mass $z \sim 3$ galaxies exhibiting broad-band colours that replicate blue high- z galaxies (see also the known real-world example of Balmer lines masquerading a Lyman break in [Donnan et al. \(2023\)](#); [Arrabal Haro et al. \(2023\)](#)).

Examining contamination in the two primary redshift bins we

explore, contamination rates are much higher for the highest redshift galaxies at $z > 10$ compared to $8 < z < 10$. These contamination rates at very high redshifts may be an overestimation, since recent JWST findings have identified greater numbers of $z > 10$ galaxies than first expected. The UV luminosity density measured from recent studies of the UV LF (e.g. [Adams et al. 2024](#); [Donnan et al. 2024](#)) is around a factor of 10 higher than JAGUAR estimations at $z \sim 10$ ([Williams et al. 2018](#)) and this discrepancy increases to higher redshift. As a result, the relative numbers of contaminant galaxies and real galaxies may differ compared to reality. The emphasis here is that contamination becomes a concerning risk at the 5–8 σ regime and that 8 σ cuts could produce more conservative/robust samples (Supporting the methods of e.g. [McLeod et al. 2024](#)).

We finally examine our two hypothetical expansions to the JOF survey design. First we explore the inclusion of the remaining 5 medium-width photometric bands (F140M, F360M, F430M, F460M, F480M). When conducting our completeness and contamination simulations, we find that contamination rates do not change compared to the current survey design. This is because the majority of these bands are at the extreme red end of NIRCcam’s wavelength coverage. For the contaminating $1.5 < z < 4$ population, emission lines are typically weak within this wavelength regime, limiting the information that medium-width bands provide. Completeness does increase for fainter sources, particularly for sources with prominent Balmer breaks at 4–5 microns. For the second hypothetical case, we increase the depths of the two bluest bands (F090W, F115W) by 0.4 mags to better match the depth of the other bands. We find this approach to be highly impactful on both completeness and contamination rates. This is because the deeper bands probing the break regime improve the limits placed on a non-detection and rule out Balmer break solutions more confidently.

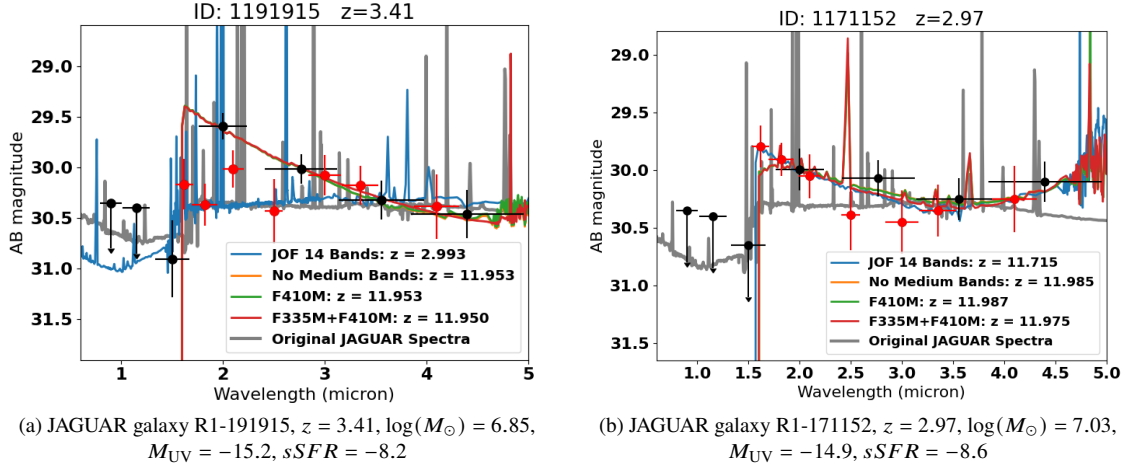


Figure 8. The SED fits applied to mock photometry of two example simulated galaxies from the JAGUAR Semi-Analytic Model which are low- z but selected as high- z with NIRCcam photometry. In all plots, the grey line shows the original JAGUAR spectra, the blue line shows the EAZY SED fit using of all 14 JOF filters and the yellow, green, red lines show results from using fewer filters. Photometric data points coloured in black are broad-width bands while those in red are medium-width, all photometric data points have had random scatter applied based on JOF field depths. Both sources show instances where strong emission lines ($H\beta$, $[OIII]$ and $H\alpha$) can mimic blue high- z galaxies in broad-band colours. The first example (left) shows a case where the inclusion of many medium bands alleviates degeneracy between high- z and low- z solutions. The second case (right) an example is shown where the inclusion of many medium bands still results in the selection of a contaminant low- z galaxy as high- z .

Our findings indicate that while medium bands can be useful, from a very-high- z perspective it is important to employ those that would be located around the anticipated low- z Balmer line alternatives to rule out contaminants. In addition, the sensitivity profile of NIRCcam has resulted in a number of surveys which have F090W and F115W depths that are notably shallower than the F200W and F277W filters used to select the rest-frame UV of ultra-high- z candidates. By placing additional time into these filters, NIRCcam is capable of obtaining simultaneous observations in the desirable medium-band in the 2.5–4 micron regime in the red, enabling the contaminant population to be tackled from both angles. Future survey designs, or extensions to current programmes, with a high- z emphasis may wish to consider dedicating more time to the above in order to maximise reliable samples near their detection limits.

5 THE IMPACT OF DEPTH ON PHOTO- Z SELECTIONS & CONTAMINATION

The JADES Origins Field not only provides a vast array of JWST filters, but also exquisite depth. In this section, we experiment with artificially degrading our imaging to match the filter and depth combinations of other JWST surveys in order to assess if high- z selection criteria behave the way it is expected, or if certain contaminant populations enter our samples. Within this experiment, we degrade the depths of our images by factors of [2,4,8]. This process is conducted through the addition of random gaussian noise which is scaled based on the original distribution of background pixel values. Background pixels are identified with the use of the segmentation map generated by SExtractor which is then further dilated by 25 pixels to ensure the faint outskirts of resolved sources are excluded. The associated error and weight maps are scaled accordingly based on the degradation factors used. These images are then rerun through our full catalogue generation and sample selection pipeline. The goal is to examine how previously high S/N sources with 14 photometric bands are now handled when fewer bands and lower S/N is available.

5.1 Local Depth calculations

The above process adds a purely Gaussian noise to the data, however the original noise in the images is not perfectly Gaussian. It is affected by the presence of artefacts in the images, contributions from undetected sources and correlated noise. Consequently, while the standard deviation of the pixel distribution increases by factors of e.g. 2, the local depths measured on the resultant images do not degrade by the ~ 0.7 mags expected but by a smaller degree, particularly at small degradation levels where other factors continue to dominate. Our degradation of factors of 2, 4, 8 result in average local depths which are 0.35, 0.77, 1.40 mags shallower on average. This shows that as the Gaussian noise becomes dominant over e.g. the correlated noise, the expected behaviour is reached.

5.2 Changes in Photometric Redshifts & Selections for High- z Sources

We begin our investigation by assessing which objects meet our full selection criteria after all photometric bands are degraded by the same level. The initial selection criteria finds 50 sources at $z > 7.5$, this decreases to 46, 21, 12 when the images are degraded by the three steps described above. The number of consistent objects between the samples generated from degraded imaging was 34, 17, 9, meaning that with each degradation step, sources were both lost and gained from the sample selection. For the remainder of this section we explore what these sources are and why their classification as robust high- z galaxies (or not) changed.

We examine the sources lost from the final sample when images are degraded. Due to the shape of the high- z luminosity function, there are more galaxies at low SNR than at high SNR, and so as the noise levels are increased, large numbers of galaxies are lost from the sample due to the constraint of requiring 5σ detection's in the rest-frame UV. 16 galaxies are lost from the sample when the images are degraded by 0.35 mags, with 14/16 retaining initial high- z solutions. A total of 10 sources are lost due to detection limits in the

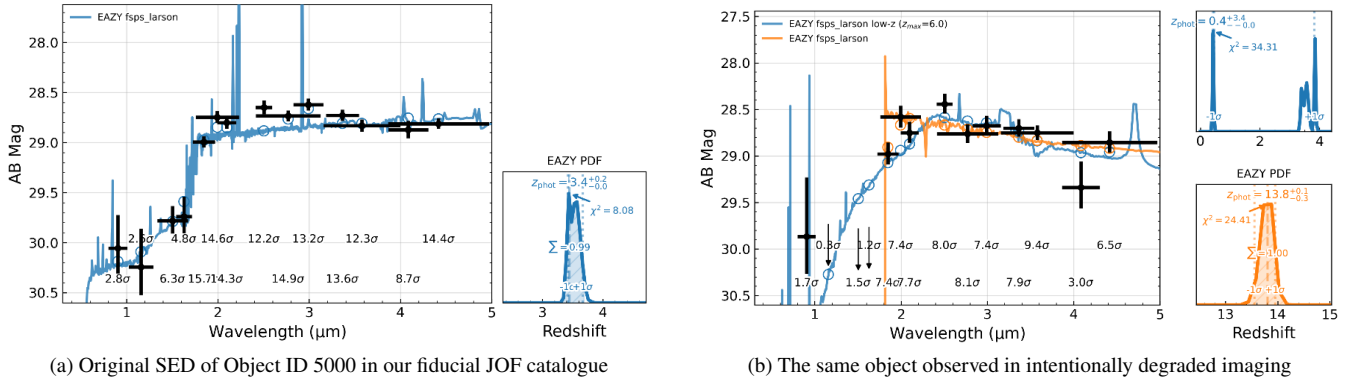


Figure 9. An example of a source identified in the original JOF imaging as a Balmer break candidate at $z = 3.4$ but is selected as a robust high- z candidate when the imaging is intentionally degraded by ~ 0.7 mags. Blue lines show the best fitting $z < 6$ solution while the orange line shows the best fitting $6 < z < 25$ solution. For the original SED fit (left) no valid high- z solution was identified. For the degraded observations (right), mild detections in the blue are removed and medium band excesses as a result of emission lines become more insignificant relative to the continuum detection, resulting in a dominant high- z solution.

rest-frame UV. For the remaining six sources, two switch to dominant low- z solutions and the other four now have too significant of a secondary solution at low- z . All six sources lost due to increasing low- z confidence have detections of less than 7σ in the degraded imaging. A similar trend is found when comparing the original catalogue to those degraded by 0.77 and 1.4 mags. Under the assumption that the photo- z is correct when using the full depth available, the completeness of high- z sources in the 5-7 σ regime in each of our degraded images is around 56-73%, broadly in line with completeness expectations from our JAGUAR simulations and slightly higher than the 40% completeness found when comparing our 0.32 and 0.2as aperture catalogues.

While many sources are lost as images are degraded in quality, there are a select few new sources that enter the sample. In total, there are 12, 3, 3 sources in each of the iterative degradations which are selected as high- z in the shallower imaging but ruled out as high- z when deeper imaging is employed. We find that there are 3,0,2 instances where the new source has no cross match in the deeper catalogue, we find these instances to be cases where in the deeper catalogue, faint and extended emission from a large resolved neighbour has blended these sources in the segmentation map. For the imaging degraded by 0.35 mags, the remaining 9 sources added to the catalogue are either classed as low redshift sources (6 objects), detected in the blue (1 object) or have poor SED statistics (2 objects). In the catalogue degraded by 0.77 mags, all 3 sources are low- z with the deeper imaging as is the 1 other object in the 1.4mag degraded catalogue.

The vast majority of sources which are selected as high- z sources in shallow catalogues but found to be confidently low- z in deeper catalogues are within the 5-8.5 σ regime in the respective shallow catalogue. Using the numbers of contaminants found, under the assumption that the photo- z using the full depth imaging is correct, the contamination rate in the 5-8.5 σ regime ranges from 20-38% between catalogues. There is a single instance of a strongly detected source 10 σ + switching from low- z in deep catalogues to high- z in shallower catalogues. This object is the spectroscopically confirmed $z = 14.32$ source (Carniani et al. 2024). It is found that the increasing background results in this source’s successful selection as the faint extended emission from its neighbour is lost to noise, creating the expected $z \sim 14$ non-detections from a Lyman dropout.

The contamination rate as measured directly from real degraded sources is slightly higher than initially anticipated from the JAGUAR

simulation work conducted in the previous sections. However, this estimation (along with the completeness value) is based on a small number of sources and highly subject to the distribution of colours and number density of potential contaminant sources. The key result here is that Balmer-Lyman confusion does take place in the 5-8 σ regime on a regular enough basis for it to be a notable concern. This is exacerbated by the relative lack of depth in the bluest bands used in deep field programmes, with 0.3+ mag differences between the depths in F090W and F115W compared to F200W a regular occurrence in deep JWST surveys. We display a full example of such a source in Figure 9.

6 MEASURING THE FAINT-END OF THE UV LUMINOSITY FUNCTION WITH THE JOF

Our findings indicate that completeness is high and contamination low for sources detected at 8 σ + in the rest-frame ultraviolet. In the context of studying galaxies as a population (e.g. by measuring the Ultraviolet Luminosity Function), the primary impact of an incorrect determination of completeness or contamination would be constrained to the faintest ~ 0.5 magnitudes probed. Other studies of the UV LF in recent literature have largely focussed on the completeness estimation and report similar findings to our own, with generally high (80 + %) completeness which rapidly falls off over a 0.3-0.5 magnitude range (See Robertson et al. 2024; Finkelstein et al. 2024, for examples). with the largest potential ramifications for the measurement of the faint-end slope ‘ α ’.

To observe the potential variability in the measurement of the UV LF, we measure the UV LF with the JOF field using the various sub-catalogues of photometric redshifts that we have produced throughout this work (different aperture sizes, different numbers of medium bands). We begin by constructing a UV LF using the base catalogue of all 14 photometric bands and 0.32as aperture diameters. We measure the UV LF using the 1/Vmax method in three redshift bins, $8.5 < z < 9.5$, $9.5 < z < 11.5$ and $11.5 < z < 13.5$, using an unmasked area of 8.7 square arcminutes. We apply the completeness correction based on the M_{UV} and redshift of each source using the JAGUAR simulations previously described and whose method is described in Adams et al. (2024). We employ a cut where no galaxies are used if their assigned completeness is below 30% or the contamination rate greater than 30%. The value of M_{UV} used

Table 3. The measured rest-frame UV LF and its error margin in the redshift bins $8.5 < z < 9.5$, $9.5 < z < 11.5$ and $11.5 < z < 13.5$. Column 1 shows the bin in absolute UV magnitude ($\lambda_{\text{rest}} = 1500\text{\AA}$), widths are set to 1 magnitude. Column 2 shows the number density of objects and column 3 shows the uncertainties in the number density, which consist of the Poisson error summed in quadrature with the derived cosmic variance from Trapp & Furlanetto (2020).

M_{UV} [mag]	$\Phi(10^{-5})$ [mag $^{-1}$ Mpc $^{-3}$]	$\delta\Phi(10^{-5})$ [mag $^{-1}$ Mpc $^{-3}$]
$z = 9$		
-20.25	7.03	6.52
-19.25	14.24	10.44
-18.25	85.30	40.00
$z = 10.5$		
-18.25	50.60	24.27
$z = 12.5$		
-18.75	19.07	12.20
$z = 9 \text{ 0.2as}$		
-20.00	7.26	6.67
-19.00	28.63	16.71
-18.50	138.6	59.29
$z = 10.5 \text{ 0.2as}$		
-18.00	60.96	29.00
$z = 12.5 \text{ 0.2as}$		
-18.50	14.30	8.91

for each source is measured by placing a 100 angstrom top hat filter between 1450-1550 angstroms in the rest-frame SED obtained during the EAZY photo- z process. These SED's are scaled up by the difference between the aperture corrected magnitude and the total magnitude from SExtractor's MAG_AUTO parameter in the nearest JWST filter to the rest-frame 1500 angstroms in order to account for light omitted due to the partly resolved nature of high- z galaxies.

Since the JOF field is limited to a single NIRCcam pointing, cosmic variance is a significant potential source of systematic bias in our measurements. To broadly estimate the impact of Cosmic variance on number counts, we utilise the cosmology calculator from Trapp & Furlanetto (2020), finding cosmic variance errors of the order 30% for the three redshift bins. This error source is added in quadrature to the Poisson error, which we calculate using the Poisson confidence interval based on the χ^2 distribution $I = [0.5\chi_{2N, a/2}^2, 0.5\chi_{2(N+1), 1-a/2}^2]$ since our number counts (N) are small in our bins (Ulm 1990).

The results of this process are presented in Figure 10. The deep imaging provided by the JOF field enables galaxies to be identified down to $M_{\text{UV}} \sim -17.5$ at $z \sim 9$ and $M_{\text{UV}} \sim -18.0$ at $z \sim 12.5$. Compared to Adams et al. (2024), which compiled 6 JWST surveys together over 180 square arcminutes of area, the JOF field expands the faint end coverage by 0.5mags. We conduct our parametric fits to the UV LF using these new JOF results, the Adams et al. (2024) results and, where possible, constraints from the ground-based UltraVISTA survey from Donnan et al. (2023). Our observations are consistent with the high number density of galaxies found by other JWST surveys that have pushed the depth frontier at $m > 30$, including the NGDEEP (Leung et al. 2023) and MIDIS surveys (Pérez-González et al. 2023).

6.1 Fitting the UV LF

To parameterise the UV LF and describe any potential evolution, it has been common process to fit the UV LF of galaxies with either a Schechter (SCH: power law with an exponential decline Schechter 1976) or Double Power Law (DPL) parameterisation. These both have a normalisation parameter (Φ^*), a characteristic luminosity/magnitude where the shape changes (M^*) and a faint-end slope (α). The DPL functional form has an additional bright-end slope (β) in replacement to the exponential decay in the Schechter form.

We elect to fit the UV LF in two different ways. First we fit with a classical χ^2 minimisation technique (Levenberg 1944; Marquardt 1963) and second we fit using a Markov-Chain-Monte-Carlo (MCMC) using emcee. When conducting our fits, we combine the measurements of this study with those from Adams et al. (2024) which mimics our methods almost identically (which also contains VISTA based-data points at the bright-end from Donnan et al. (2023)). Each MCMC run is conducted with 500 walkers, burns-in for 5000 steps and conducts an additional 5000 steps. Due to the still relative lack of galaxies at these high redshifts and the degeneracies between parameters within these functional forms, we conduct fits with all parameters left free at $z = 9$, at $z = 10.5$ we experiment with leaving all variables free and with fixing the faint-end slope to $\alpha = -2.1$. At $z = 12.5$, we fix the shape broadly to the $z = 10.5$ result and only fit for the normalisation. The value of $\alpha = -2.1$ is chosen as when it is left free at $z = 9$ and $z = 10.5$, the best fit values are typically in the range of $-2.2 < \alpha < -2.0$ in agreement with recent predictions from Donnan et al. (2025) and other observational studies using JWST and HST, though still with relatively large error margins.

Relative to results from Adams et al. (2024), uncertainties in the faint-end slopes (when left free) have decreased by around 25-30% thanks to the increased depth provided by the JOF field allowing us to identify intrinsically fainter galaxies ($\sim 0.5\text{mags}$).

6.2 A consistent faint-end of the UV LF between photometric catalogues

We repeat the above procedure for measuring the UV LF with four other versions of our photometric catalogue. The first three use the same 0.32as aperture data, but omit medium-width bands leaving only zero, F410M or F410M+F335M bands available, mimicking the bands used in similar deep field JWST surveys. We found in Section 4 that between catalogues that employ different combinations of medium-width bands, the number of selected sources at $z > 8$ varies by only $\sim 10\%$ and that the anticipated completeness also varies by of order 10-15%. Therefore differences between UV LF's measured by the different catalogues may be expected to be consistent.

We find that for the $z = 9$ and $z = 10.5$ UV LF, the majority of galaxies used are consistent between the C-ALL, C-0, C-1 and C-2 catalogues, though up to 20% of the galaxies occupying the faintest bin can change. These galaxies fall into two categories; 1) they either have a photo- z close to the redshift bin boundary which changes slightly between catalogues (e.g. $z_p = 8.6$ in the $8.5 < z < 9.5$ bin) scattering them in/out or 2) they are among the faintest in the sample and are no longer selected due to changes in χ^2 confidence relative to low- z solutions in different catalogues. For the $z = 12.5$ redshift bin, the C-ALL catalogue employs the use of 3 galaxies, while C-2 and C-1 use 1 galaxy and C-0 uses no galaxies. The scatter in redshift is larger in this regime, with two $z \sim 12$ galaxies in C-ALL now $z \sim 11$ or $z \sim 14$ in C-0. Additionally, completeness and contamination are

Table 4. The best-fit parameters for the final Schechter (Sch) and Double Power Law (DPL) functional forms for both the Levenberg–Marquard (LM) approach and the MCMC approach when applied to our deeper 0.2as catalogue with all available bands. For the MCMC, we show the median and standard error obtained from the posterior. The individual MCMC sample with highest probability closely matches the best fitting parameters of the LM methodology. Values presented with an asterisk indicate the parameter is fixed to this value in the fitting procedure.

Redshift	Method	$\log 10(\Phi)$	M^*	α	β
9	Sch/LM	-3.84 ± 0.58	$-20.31 - \pm 0.57$	-2.08 ± 0.46	–
9	Sch/MCMC	$-3.99^{+0.59}_{-0.88}$	$-20.41^{+0.62}_{-0.81}$	$-2.17^{+0.61}_{-0.47}$	–
9	DPL/LM	-4.32 ± 0.55	-20.76 ± 0.54	-2.24 ± 0.40	-5.7 ± 2.1
9	DPL/MCMC	$-4.16^{+0.48}_{-0.66}$	$-20.51^{+0.61}_{-0.54}$	$-2.21^{+0.53}_{-0.44}$	$-4.80^{+0.75}_{-0.77}$
10.5	Sch/LM	-4.71 ± 0.51	-20.98 ± 0.52	-2.04 ± 0.40	–
10.5	Sch/MCMC	$-4.65^{+0.55}_{-0.93}$	$-20.81^{+0.74}_{-0.87}$	$-2.04^{+0.56}_{-0.50}$	–
10.5	DPL/LM	-5.26 ± 1.16	-21.44 ± 1.46	-2.30 ± 0.45	-5.2 ± 3.8
10.5	DPL/MCMC	$-4.88^{+0.63}_{-0.81}$	$-20.86^{+0.88}_{-0.85}$	$-2.20^{+0.59}_{-0.45}$	$-4.45^{+0.94}_{-1.02}$
10.5	Sch/LM	-4.77 ± 0.21	-21.04 ± 0.29	-2.1^*	–
10.5	Sch/MCMC	$-4.73^{+0.30}_{-0.26}$	$-20.93^{+0.49}_{-0.33}$	-2.1^*	–
10.5	DPL/LM	-4.89 ± 0.40	-21.00 ± 0.65	-2.1^*	-4.55 ± 1.21
10.5	DPL/MCMC	$-4.83^{+0.41}_{-0.32}$	$-20.83^{+0.67}_{-0.51}$	-2.1^*	$-4.62^{+0.90}_{-0.91}$
12.5	Sch/LM	-4.80 ± 0.14	-21.0^*	-2.1^*	–
12.5	Sch/MCMC	$-4.87^{+0.15}_{-0.27}$	-21.0^*	-2.1^*	–
12.5	DPL/LM	-4.94 ± 0.14	-21.0^*	-2.1^*	-4.6^*
12.5	DPL/MCMC	$-5.01^{+0.15}_{-0.26}$	-21.0^*	-2.1^*	-4.6^*

also sensitive. For C-ALL, the average completeness is 83% for the galaxies used while it drops to 40% for C-2 and C-1, with this factor of two in completeness making up some of the difference in measured number density obtained from using 1 or 3 galaxies.

The four catalogue iterations (C-ALL, C-0, C-1, C-2) all produce consistent UV LFs when errors from poisson statistics and cosmic variance are considered, though these error sources are large. A wider area medium-band study would be required to elaborate further. Our findings agree with earlier JWST-based work that pushed the $m > 30$ boundary and found high number densities of moderately luminous ($-19 < M_{UV} < -18$) galaxies both within this very field (Robertson et al. 2024) and in other fields (Leung et al. 2023; Pérez-González et al. 2023).

When using a different aperture size, we also observe minor changes to the measured UV LF that match expectations. The deeper coverage provided by the use of smaller apertures enables intrinsically fainter galaxies (0.25–0.5 mags) to be identified while the brighter galaxies found in the wider aperture catalogue have the majority recovered with similar redshifts and properties. We provide the final UV LF fits to the 0.2as version of the UV LF on account of its constraining power on the faint-end slope in Table 4 and provide the points in Table 3.

6.3 The UV Luminosity Density

Using our fiducial UV LF measurement, we calculate the UV Luminosity density down to $M_{UV} < -17$ by integrating 1000 randomly drawn samples from the MCMC chains. This is then converted into an estimated star formation rate density (SFRD) replicating the procedure of Harikane et al. (2023) and Adams et al. (2024). Here, we use the relations presented in Madau & Dickinson (2014), obtaining a conversion factor $k = 1.15 \times 10^{-28} [M_{\odot} \text{yr}^{-1} / (\text{erg s}^{-1} \text{Hz}^{-1})]$. The results of this process are presented in Figure 11. The key result here is that the high number density of observed galaxies at $-19 < M_{UV} < -18$ galaxies at $z > 10$ have constrained the previously uncertain UV Luminosity Density at $z \sim 12$ to the upper bound of our previous measurements in Adams et al. (2024), resulting in

a greater tension with a selection of models which predict relatively low numbers of high- z galaxies.

When fitting a trivial log-linear evolution (e.g. Donnan et al. 2023; McLeod et al. 2024; Donnan et al. 2024) to our updated UV luminosity density measurements (including the $z = 8$ result from Adams et al. 2024), we find a slope of -0.26 ± 0.04 and normalisation of 27.73 ± 0.26 . The steepness of this evolution is shallower than initially measured in Adams et al. (2024), closer to the value measured by McLeod et al. (2024) but steeper than found in Donnan et al. (2024). When compared to theoretical predictions, there is a general bimodality in the star formation rate density expected, with a selection of simulations and analytic prescriptions predicting low star formation rates (SCSAM Yung et al. 2024), Thesan Kannan et al. (2022), UniverseMachine Behroozi et al. (2019) in addition to Harikane et al. (2022)) and a selection predicting higher (FLARES Wilkins et al. (2023), Delphi Dayal et al. (2022), Ferrara et al. (2023) in addition to Behroozi & Silk (2015)). At $z = 10$, our observations more closely match to those predicting lower SFRD, while at $z = 12$ the opposite is the case, with observations more closely matching predictions of high SFRD. Further increased volume and sightlines probing fainter luminosities (e.g. the complete JADES survey and lensing clusters from e.g. PEARLS, CANUCS and GLIMPSE) will ultimately be required in order fully constrain the shape of the UV LF at $z > 10$ and $-19 < M_{UV} < -16$.

7 CONCLUSIONS

In this paper, we use the recently conducted JADES Origins Field survey, in parallel with the JAGUAR semi-analytic simulation, to conduct an assessment of the completeness and contamination rates when photometrically selecting the highest redshift galaxies at $z > 8$ with JWSTs NIRCcam. We explore the advantage that the addition of medium-width photometric filters provides and intentionally degrade imaging to observe how selections differ as SNR values decrease. We also measure the resulting UV luminosity function using our methods to determine the best measurement possible at these depths in the JOF and how other realisations of the galaxy population would

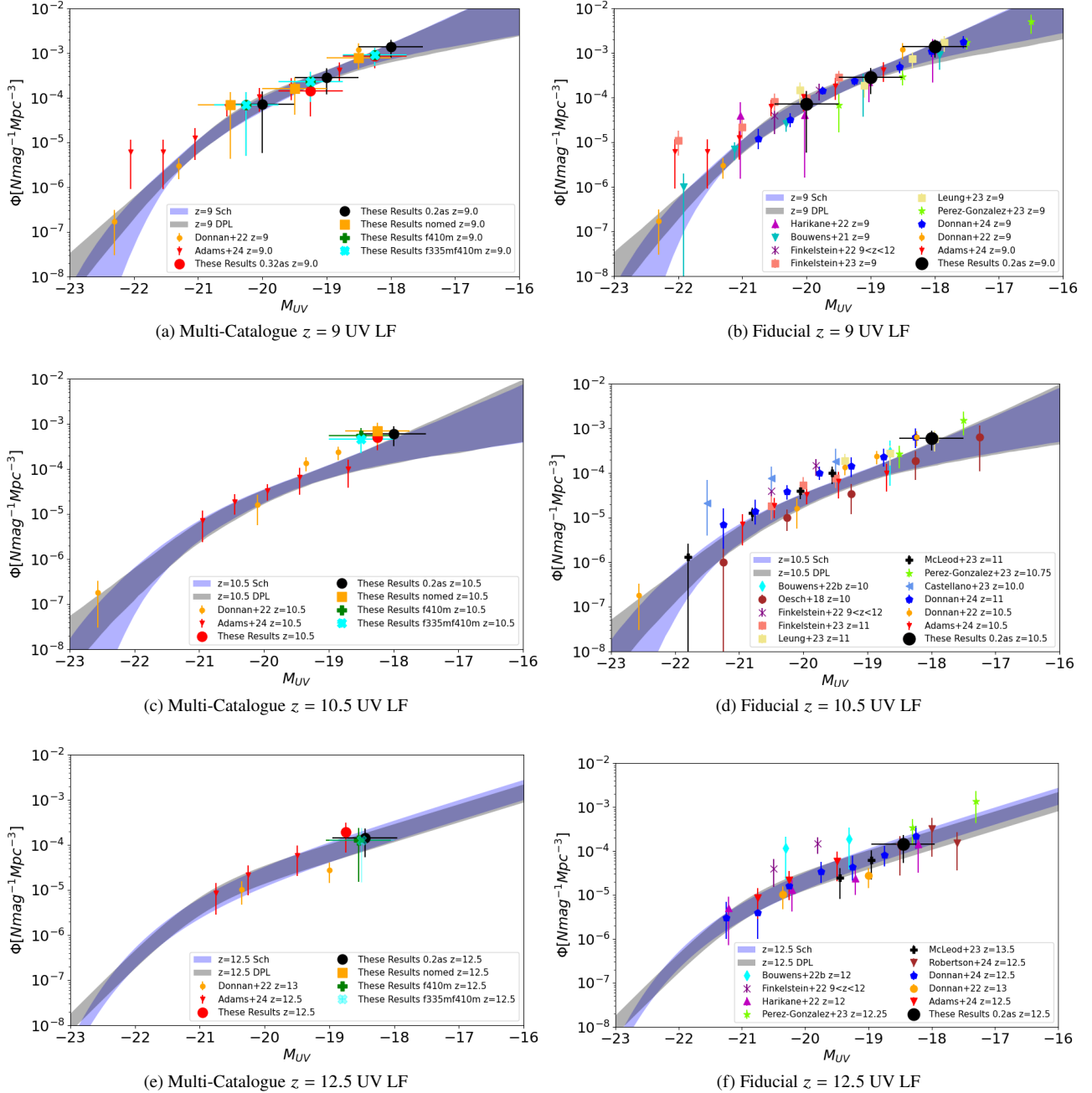


Figure 10. The measured faint end of the UV Luminosity function within the redshift bins of $8.5 < z < 9.5$, $9.5 < z < 11.5$ and $11.5 < z < 13.5$. In the left column, we show the results from using either the 0.32as aperture catalogue, the 0.2as aperture catalogue or removing medium bands from the process. Various interpretations are found produce consistent results with the anticipated behaviour of the 0.2as catalogue extending the luminosity range faintwards. Shaded regions indicate the 1σ confidence interval on the best fit Schechter or DPL function to the fiducial UV LF (0.2as apertures plus the use of Adams et al. (2024) and bright VISTA data points from Donnan et al. (2023)). In the right column, we show our fiducial result alongside the range of previous observations using HST and JWST. These include: (Oesch et al. 2018; Harikane et al. 2023; Bouwens et al. 2021, 2022; Donnan et al. 2023; Finkelstein & Bagley 2022; Finkelstein et al. 2024; Leung et al. 2023; Pérez-González et al. 2023; Adams et al. 2024; McLeod et al. 2024; Donnan et al. 2024; Robertson et al. 2024)

affect this. Following these experiments, we identify the follow key conclusions:

(i) Even without the use of any medium-width bands, sample completeness is generally high (80%+ at 10σ +). As the number of medium-width bands increases, so does sample completeness alongside a decrease in contamination. Medium width bands are most

effective in decreasing contamination when they probe central NIR-Cam wavelengths (2-3.5 microns) where they cover the expected locations of emission lines for contaminant low- z sources (Balmer and Oxygen lines).

(ii) A drop off in completeness rates and an increase in contamination rates begin to occur when probing the luminosity regime where

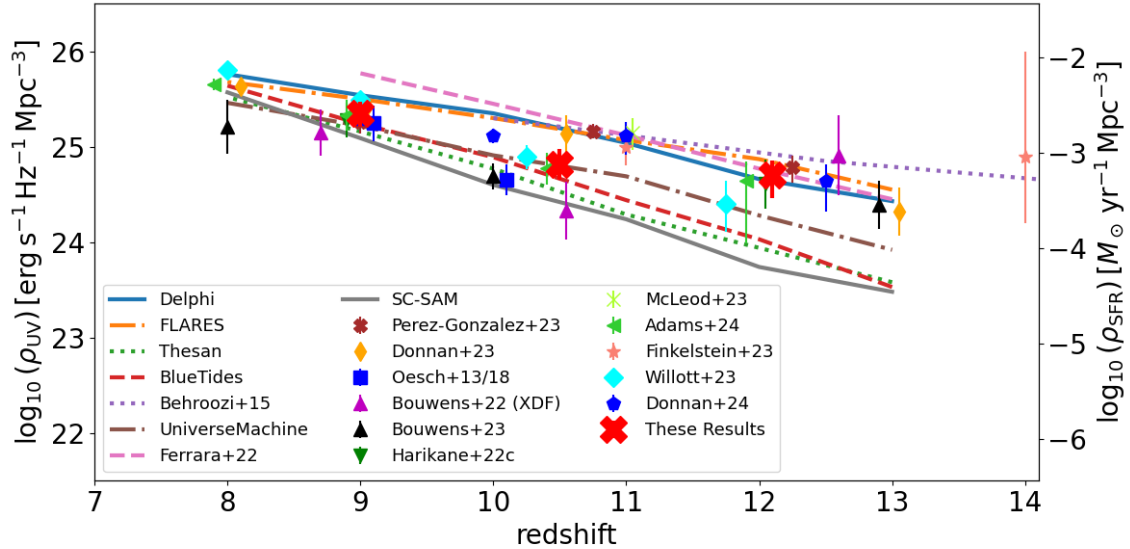


Figure 11. The measured UV Luminosity density and star formation rate density at $8 < z < 14$ from a compilation of HST and JWST-based studies plotted over the predictions from a selection of simulations and semi-analytical models. Observations include Oesch et al. (2013, 2018); Donnann et al. (2023); Bouwens et al. (2022); Pérez-González et al. (2023); Donnann et al. (2024); Harikane et al. (2023); McLeod et al. (2024); Finkelstein et al. (2024); Willott et al. (2024); Adams et al. (2024). Predictions include those from Delphi (Dayal et al. 2022), FLARES (Wilkins et al. 2023), Thesan (Kannan et al. 2022), BlueTides (Marshall et al. 2022), SC-SAM Yung et al. (2024), Behroozi & Silk (2015), UniverseMachine (Behroozi et al. 2019), Ferrara et al. (2023). At $8 < z < 9$ observations are in close agreement with each other, while at $z \sim 10 - 11$ the spread increases to span the full range of predictions before re-concentrating at $z > 12$ around higher SFRD.

the rest-frame UV is less than 8σ . This is caused by an increasing degeneracy between Lyman and Balmer break solutions, exacerbated by the generally shallower blue photometric bands (F090W and F115W) common in deep field surveys due to NIRCcam’s sensitivity profile. This enables sources to be detected in the anticipated rest-frame UV at depths often fainter than the 5σ limits of the neighbouring bands probing the Lyman break.

(iii) Degrading JOF images results in changes to the selected high- z sample broadly following the expectations of our simulation work. Completeness falls off in the $5-7\sigma$ regime as previously high- z sources are now degenerate with Balmer break solutions. In addition, small numbers of low- z Balmer break sources with minor blue detections in the original imaging can be selected as high- z sources when images are degraded to be shallower. Completeness in the faint regime is measured from degraded imaging to be around 56-73%, broadly agreeing with our simulated estimates, while contamination is slightly higher than expected at 20-38%, through it is measured using a small number of sources.

(iv) Instances of selecting contaminant sources can be alleviated through the use of medium-width bands positioned where low- z emission lines are to be expected and through an increase in observing time spent on the bluest photometric bands. The modular design of NIRCcam is advantageous in this regard, since doubling the time spent in the bluest bands can be conducted in parallel to obtaining some of the redder medium-width bands. In the event that early JWST surveys are expanded upon or new fields contributed, we recommend the inclusion of additional time in the blue broad-bands relative to the red broad-bands in order to maximise the utility of the depths the red broad-width bands can achieve.

(v) Our fiducial measurement of the faint end of the UV LF at redshifts 8.5 to 13.5 agree with previous estimates from early JWST data, evidencing high numbers of moderately faint galaxies ($M_{UV} \sim -18.5$) at this early time. The estimated star formation rate density of

the Universe at $z = 12$ is higher than previously measured in Adams et al. (2024) and closer to other early JWST-based measurements.

(vi) When reproducing UV LF measurements using different catalogues that employ different combinations of photometric bands, we find no significant difference in the obtained results. Indicating that an adequate understanding of sample completeness and contamination can enable large, statistical studies to be reliably conducted with broad-band dominated surveys.

We have shown that medium-width photometric bands can improve the reliability of photo- z ’s for the faintest high- z targets in the $5-8\sigma$ regime. When studying and following up the deepest fields at $m > 30$, they may prove crucial to identifying targets before significant time investment from spectroscopy or other follow-up work is committed. There is concern is that faint, dusty and/or low-mass Balmer break sources can mimic the colours of Lyman break galaxies in many early JWST survey designs (see also discussion in Gandolfi et al. 2025). There are now several medium-band programmes already planned, underway or completed (e.g. JEMS, MegaScience, Technicolour, JUMPS) which will continue to pave the path forwards and open avenues to study extreme emission line systems, high- z drop outs and further stress-test photo- z pipelines.

It is also worth stressing that development continues to improve high- z selections. This work displays the expected reliability and issues facing currently employed systems. New templates of galaxy SEDs are continuously being tested (e.g. Larson et al. 2023; Clausen et al. 2024), understanding of IGM attenuation is improving (e.g. Asada et al. 2024) and the application of informed priors can be used to more conservatively examine fainter sources (e.g. Donnann et al. 2024). Increasing spectroscopic samples of populations which can masquerade as high- z galaxies (be it galactic brown dwarfs, dusty line emitters or Balmer break galaxies) or objects occupying unexplored parameter spaces (e.g. RUBIES de Graaff et al. 2024) will be pivotal to refining high redshift selections and SED template sets.

With large spectroscopic programmes like JADES, and now with CAPERS underway, a more statistical analysis of SED modelling comparing to real spectra will soon be enabled.

ACKNOWLEDGEMENTS

We acknowledge support from the ERC Advanced Investigator Grant EPOCHS (788113), as well as two studentships from the STFC. JAAT acknowledges support from the Simons Foundation and JWST program 3215. Support for program 3215 was provided by NASA through a grant from the Space Telescope Science Institute, which is operated by the Association of Universities for Research in Astronomy, Inc., under NASA contract NAS 5-03127.

This work is based on observations made with the NASA/ESA *Hubble Space Telescope* (HST) and NASA/ESA/CSA *James Webb Space Telescope* (JWST) obtained from the Mikulski Archive for Space Telescopes (MAST) at the *Space Telescope Science Institute* (STScI), which is operated by the Association of Universities for Research in Astronomy, Inc., under NASA contract NAS 5-03127 for JWST, and NAS 5-26555 for HST. The authors thank all involved with the construction and operation of JWST, without whom this work would not be possible. The authors also thank the team who designed and proposed for the JADES (PID 1280,1287) and JADES Origins Field (PID 3215) observing programmes, whose data was used in this study. Elements of this work also used observational products from CANUCS, GLASS, CEERS, FRESCO, JEMS, NGDEEP, PEARLS and MegaScience JWST surveys. We thank all of those involved in these collaborations for their efforts in designing and carrying out these observations.

This work makes use of astropy (Astropy Collaboration et al. 2013, 2018, 2022), matplotlib (Hunter 2007), reproject, DrizzlePac (Hoffmann et al. 2021), SciPy (Virtanen et al. 2020), msaexp <https://zenodo.org/records/7579050> and photutils (Bradley et al. 2022) and the galfind photometric toolbox <https://github.com/duncanaustin98/galfind>. The authors thank Anthony Holloway and Sotirios Sanidas for providing their expertise in high performance computing and other IT support throughout this work. We also thank Elizabeth Stanway, Stephen Wilkins and Joseph Caruana for their helpful discussions. Some of the data products presented herein were retrieved from the Dawn JWST Archive (DJA). DJA is an initiative of the Cosmic Dawn Center (DAWN), which is funded by the Danish National Research Foundation under grant DNRF140.

DATA AVAILABILITY

This work makes use of raw data from the JADES GTO survey programme ID's 1280, 1287 and the Jades Origins Field GO programme 3215. All raw data was obtained from the MAST portal operated by STScI, a DOI linking to the data is provided here: DOI [10.17909/a2e3-bj58](https://doi.org/10.17909/a2e3-bj58)

Templates for the Wisp artefact which were generated in this work utilised JWST STAGE 2 calibrated products from programmes: 1180 (JADES, PI: D. Eisenstein Eisenstein et al. 2023a; Bunker et al. 2024; Rieke et al. 2023; Eisenstein et al. 2023c; Hainline et al. 2024), 1208 (CANUCS, PI: C. Willott; Willott et al. 2024), 1210 (JADES, PI: N. Luetzendorf), 1324 (GLASS, PI: T. Treu; Treu et al. 2022; Mascia et al. 2024), 1345 (CEERS, PI: S. Finkelstein; Bagley et al. 2023; Finkelstein et al. 2024), 1895 (FRESCO, PI: P. Oesch; Oesch et al. 2023), 1963 (JEMS, PI: C. Williams; Williams et al. 2023), 2079

(NGDEEP, PI: S. Finkelstein; Bagley et al. 2024), 2738 (PEARLS, PI: R. Windhorst; Windhorst et al. 2023), 3215 (JOF, PI: D. Eisenstein; Eisenstein et al. 2023b; Robertson et al. 2024), 4111 (MegaScience, PI: K. Suess; Suess et al. 2024). The final product is made available on the following cloud-based repository: <https://1drv.ms/f/s!AjXt-wkeMSXAgr1I7h5rQUe-Lx2rpA?e=IxpN6M>

If the reader is interested in any other products from this work (images, catalogues etc.) they are welcome to contact the lead author.

REFERENCES

- Adams N. J., et al., 2024, *ApJ*, 965, 169
 Arrabal Haro P., et al., 2023, *Nature*, 622, 707
 Asada Y., et al., 2024, arXiv preprint arXiv:2410.21543
 Astropy Collaboration et al., 2013, *A&A*, 558, A33
 Astropy Collaboration et al., 2018, *AJ*, 156, 123
 Astropy Collaboration et al., 2022, *ApJ*, 935, 167
 Austin D., et al., 2024, arXiv e-prints, p. arXiv:2404.10751
 Bagley M. B., et al., 2023, *ApJ*, 946, L12
 Bagley M. B., et al., 2024, *ApJ*, 965, L6
 Balestra I., et al., 2010, *A&A*, 512, A12
 Barrufet L., et al., 2024, arXiv e-prints, p. arXiv:2404.08052
 Behroozi P. S., Silk J., 2015, *ApJ*, 799, 32
 Behroozi P., Wechsler R. H., Hearin A. P., Conroy C., 2019, *MNRAS*, 488, 3143
 Bouwens R. J., et al., 2021, *AJ*, 162, 47
 Bouwens R. J., et al., 2022, *ApJ*, 931, 160
 Bradley L., et al., 2022, astropy/photutils: 1.5.0, doi:10.5281/zenodo.6825092, <https://doi.org/10.5281/zenodo.6825092>
 Brammer G. B., van Dokkum P. G., Coppi P., 2008, *ApJ*, 686, 1503
 Bunker A. J., et al., 2024, *A&A*, 690, A288
 Calzetti D., Armus L., Bohlin R. C., Kinney A. L., Koornneef J., Storchi-Bergmann T., 2000, *ApJ*, 533, 682
 Carniani S., et al., 2024, *Nature*, 633, 318
 Clausen T., Steinhardt C. L., Shao A., Senthil Kumar G., 2024, arXiv e-prints, p. arXiv:2412.01893
 Coe D., et al., 2012, *ApJ*, 757, 22
 Conselice C. J., et al., 2024, arXiv e-prints, p. arXiv:2407.14973
 Cooper M. C., et al., 2012, *MNRAS*, 425, 2116
 Curtis-Lake E., et al., 2023, *Nature Astronomy*, 7, 622
 D'Eugenio F., et al., 2024, arXiv e-prints, p. arXiv:2404.06531
 Dayal P., et al., 2022, *MNRAS*, 512, 989
 Donnan C. T., et al., 2023, *MNRAS*, 518, 6011
 Donnan C. T., et al., 2024, *MNRAS*, 533, 3222
 Donnan C. T., Dunlop J. S., McLure R. J., McLeod D. J., Cullen F., 2025, arXiv e-prints, p. arXiv:2501.03217
 Eisenstein D. J., et al., 2023a, arXiv e-prints, p. arXiv:2306.02465
 Eisenstein D. J., et al., 2023b, arXiv e-prints, p. arXiv:2310.12340
 Eisenstein D. J., et al., 2023c, arXiv e-prints, p. arXiv:2310.12340
 Ferrara A., Pallottini A., Dayal P., 2023, *MNRAS*, 522, 3986
 Finkelstein S. L., Bagley M. B., 2022, arXiv e-prints, p. arXiv:2207.02233
 Finkelstein S. L., et al., 2024, *ApJ*, 969, L2
 Gaia Collaboration et al., 2023, *A&A*, 674, A1
 Gandolfi G., et al., 2025, arXiv e-prints, p. arXiv:2502.02637
 Garilli B., et al., 2021, *A&A*, 647, A150
 Giardino G., et al., 2022, in Coyle L. E., Matsuura S., Perrin M. D., eds, Society of Photo-Optical Instrumentation Engineers (SPIE) Conference Series Vol. 12180, Space Telescopes and Instrumentation 2022: Optical, Infrared, and Millimeter Wave. p. 121800X (arXiv:2208.04876), doi:10.1117/12.2628980
 Hainline K. N., et al., 2020, *ApJ*, 892, 125
 Hainline K. N., et al., 2024, *ApJ*, 964, 71
 Harikane Y., et al., 2022, *ApJ*, 929, 1
 Harikane Y., et al., 2023, *ApJS*, 265, 5
 Harvey T., et al., 2025, *ApJ*, 978, 89

Heintz K. E., et al., 2024, [arXiv e-prints](#), p. [arXiv:2404.02211](#)

Hoffmann S. L., Mack J., Avila R., Martlin C., Cohen Y., Bajaj V., 2021, in American Astronomical Society Meeting Abstracts. p. 216.02

Holwerda B. W., et al., 2024, [MNRAS](#), **529**, 1067

Hunter J. D., 2007, [Computing in Science & Engineering](#), 9, 90

Kannan R., Garaldi E., Smith A., Pakmor R., Springel V., Vogelsberger M., Hernquist L., 2022, [MNRAS](#), **511**, 4005

Kauffmann O. B., et al., 2020, [A&A](#), **640**, A67

Kokorev V., et al., 2024, [arXiv e-prints](#), p. [arXiv:2401.09981](#)

Labbé I., et al., 2023, [Nature](#), 616, 266

Larson R. L., et al., 2023, [ApJ](#), **958**, 141

Le Fèvre O., et al., 2015, [A&A](#), **576**, A79

LeFèvre O., et al., 2013, [A&A](#), 559, A14

Leung G. C. K., et al., 2023, [ApJ](#), **954**, L46

Levenberg K., 1944, *Quarterly of Applied Mathematics*, 2, 164

Madau P., 1995, [ApJ](#), **441**, 18

Madau P., Dickinson M., 2014, [ARA&A](#), **52**, 415

Marley M. S., et al., 2021, [ApJ](#), **920**, 85

Marquardt D. W., 1963, *Journal of the Society for Industrial and Applied Mathematics*, 11, 431

Marshall M. A., et al., 2022, [MNRAS](#), **516**, 1047

Mascia S., et al., 2024, [A&A](#), **690**, A2

Matthee J., et al., 2023, [arXiv preprint arXiv:2306.05448](#)

McLeod D. J., et al., 2024, [MNRAS](#), **527**, 5004

Merlin E., et al., 2021, [A&A](#), **649**, A22

Momcheva I. G., et al., 2016, [ApJS](#), **225**, 27

Morris A. M., et al., 2015, [AJ](#), **149**, 178

Oesch P. A., et al., 2013, [ApJ](#), **773**, 75

Oesch P. A., Bouwens R. J., Illingworth G. D., Labbé I., Stefanon M., 2018, [ApJ](#), **855**, 105

Oesch P. A., et al., 2023, [MNRAS](#), **525**, 2864

Pérez-González P. G., et al., 2023, [ApJ](#), **951**, L1

Perrin M. D., Soummer R., Elliott E. M., Lallo M. D., Sivaramakrishnan A., 2012, in Clampin M. C., Fazio G. G., MacEwen H. A., Oschmann Jacobus M. J., eds, *Society of Photo-Optical Instrumentation Engineers (SPIE) Conference Series Vol. 8442, Space Telescopes and Instrumentation 2012: Optical, Infrared, and Millimeter Wave*. p. 84423D, [doi:10.1117/12.925230](#)

Perrin M. D., Sivaramakrishnan A., Lajoie C.-P., Elliott E., Pueyo L., Ravindranath S., Albert L., 2014, in Oschmann Jacobus M. J., Clampin M., Fazio G. G., MacEwen H. A., eds, *Society of Photo-Optical Instrumentation Engineers (SPIE) Conference Series Vol. 9143, Space Telescopes and Instrumentation 2014: Optical, Infrared, and Millimeter Wave*. p. 91433X, [doi:10.1117/12.2056689](#)

Price S. H., et al., 2024, [arXiv e-prints](#), p. [arXiv:2408.03920](#)

Ravikumar C. D., et al., 2007, [A&A](#), **465**, 1099

Rieke M. J., et al., 2023, [ApJS](#), **269**, 16

Robertson B., et al., 2024, [ApJ](#), **970**, 31

Robotham A. S. G., D’Silva J. C. J., Windhorst R. A., Jansen R. A., Summers J., Driver S. P., Wilmer C. N. A., Bellstedt S., 2023, [PASP](#), **135**, 085003

Schechter P., 1976, [ApJ](#), **203**, 297

Suess K. A., et al., 2024, [ApJ](#), **976**, 101

Szokoly G. P., et al., 2004, [ApJS](#), **155**, 271

Trapp A. C., Furlanetto S. R., 2020, [MNRAS](#), **499**, 2401

Treu T., et al., 2022, [ApJ](#), **935**, 110

Ulm K., 1990, [American Journal of Epidemiology](#), 131, 373

Vanzella E., et al., 2008, [A&A](#), **478**, 83

Virtanen P., et al., 2020, [Nature Methods](#), 17, 261

Wang B., et al., 2023, [ApJ](#), **957**, L34

Weaver J. R., et al., 2024, [ApJS](#), **270**, 7

Whitaker K. E., et al., 2019, [ApJS](#), **244**, 16

Wilkins S. M., et al., 2023, [arXiv e-prints](#), p. [arXiv:2311.08065](#)

Williams C. C., et al., 2018, [ApJS](#), **236**, 33

Williams C. C., et al., 2023, [ApJS](#), **268**, 64

Willott C. J., et al., 2024, [ApJ](#), **966**, 74

Windhorst R. A., et al., 2023, [AJ](#), **165**, 13

Yung L. Y. A., Somerville R. S., Finkelstein S. L., Wilkins S. M., Gardner J. P., 2024, [MNRAS](#), **527**, 5929

Zavala J. A., et al., 2023, [ApJ](#), **943**, L9

de Graaff A., et al., 2024, [arXiv preprint arXiv:2409.05948](#)

APPENDIX A: FULL LIST OF HIGH-Z GALAXY CANDIDATES

In this appendix, we provide a full table of the high redshift galaxies selected in our ‘final’ sample (catalogues using the full number of NIRCcam bands available). We highlight which objects were previously identified in [Robertson et al. \(2024\)](#) as well as which objects are selected in only the 0.2as aperture version of our SED fits. Below the table, we show a selection of example SED fits across the full redshift range considered.

Table A1: The full tabulated list of selected high- z targets in the JADES Origins Field. The first set of objects consist of those selected in the fiducial 0.32as aperture catalogue. The second set of objects show which objects are added when smaller 0.2as apertures are implemented. Shown are the best fit photometric redshift, photo- z at either side 1σ value, the total M_{UV} , aperture corrected F277W magnitude and the next best-fitting low- z solution at $z < 6$. Values of -1.0 indicate a failure to obtain a solution.

EPOCHS ID	RA	DEC	zphot	zphot_16	zphot_84	χ^2	MUV	F277W	σ_{F277W}	zphot($z < 6$)	$\chi^2_{z < 6}$
10536	53.07332	-27.85679	7.56	7.31	7.74	11.38	-18.08	29.52	7.92	1.50	52.28
9995	53.03078	-27.88841	7.57	7.28	7.59	9.36	-18.00	29.08	15.45	1.50	54.36
295	53.07920	-27.88182	7.65	7.60	7.71	14.83	-17.96	29.30	9.29	0.29	28.07
711	53.03645	-27.91106	7.82	7.75	7.95	7.21	-18.38	29.43	13.35	1.51	41.66
6475	53.09007	-27.85577	7.82	7.45	8.08	9.51	-17.60	29.70	6.30	1.50	20.29
1694	53.09918	-27.86335	7.83	7.76	8.23	20.18	-17.82	29.71	7.48	1.74	35.56
2808	53.07720	-27.87574	7.87	7.02	7.97	26.45	-18.16	29.11	10.22	1.65	37.99
9036	53.04792	-27.87873	7.93	7.86	8.06	2.41	-19.56	28.04	32.94	1.71	77.45
9091	53.06998	-27.86297	7.93	7.85	8.36	24.65	-17.61	29.85	7.10	2.35	35.70
11076	53.04431	-27.87622	7.93	7.78	8.15	7.87	-18.16	29.36	10.39	1.47	24.19
7540	53.08745	-27.85464	7.97	7.87	8.20	3.30	-19.01	28.56	17.26	1.70	61.79
4143	53.08222	-27.86811	7.98	7.90	8.04	14.40	-18.79	28.89	15.02	1.69	49.17
5532	53.08741	-27.86040	8.03	7.92	8.10	4.88	-19.73	27.81	35.26	1.70	109.27
7893	53.05373	-27.87789	8.08	8.00	8.20	6.27	-19.91	27.71	41.98	1.72	104.74
6492	53.03579	-27.89471	8.10	7.99	8.21	6.06	-18.09	29.50	10.21	1.70	41.27
7389	53.07052	-27.86725	8.12	7.96	8.27	2.15	-19.73	27.83	40.93	1.71	90.51
15589	53.07027	-27.84822	8.19	7.93	8.33	14.95	-18.08	29.50	7.51	1.50	47.74
6157	53.08678	-27.85915	8.21	7.99	8.28	20.08	-18.99	28.66	15.68	-1.00	-1.00
5671	53.03334	-27.89862	8.26	8.14	8.36	19.05	-18.81	28.40	20.45	1.91	46.23
893	53.08932	-27.87269	8.26	8.18	8.35	5.56	-19.63	27.93	36.71	1.70	127.18
2171	53.10223	-27.85925	8.29	8.18	8.44	2.46	-19.93	27.95	34.21	1.70	108.31
6108	53.08650	-27.85920	8.32	8.22	8.40	19.25	-19.82	27.52	46.03	1.74	64.50
3888	53.10441	-27.85305	8.32	8.23	8.40	21.95	-18.40	29.12	11.29	-1.00	-1.00
5371	53.08739	-27.86032	8.32	8.19	8.40	7.34	-20.60	27.40	50.63	1.94	87.59
966	53.03657	-27.91026	8.37	8.09	8.53	6.81	-17.91	29.68	10.69	2.36	24.23
3400	53.03385	-27.90509	8.46	8.27	8.60	2.67	-18.58	29.22	10.95	1.89	51.71
3639	53.09238	-27.86232	8.46	8.35	8.58	9.88	-19.06	28.46	24.17	2.01	42.25
10090	53.08105	-27.85234	8.54	8.18	8.76	23.73	-17.81	29.69	7.36	2.36	42.42
8958	53.07037	-27.86308	8.57	8.35	8.72	16.85	-18.10	29.45	10.08	1.89	54.45
1685	53.09686	-27.86504	8.57	8.42	8.70	4.17	-18.87	28.85	14.64	2.05	57.50
3823	53.05999	-27.88514	8.62	8.48	8.77	6.19	-18.53	29.30	11.42	0.20	25.24
15476	53.06717	-27.84728	8.68	8.53	8.82	4.49	-18.64	29.03	12.73	2.18	61.84
2267	53.05414	-27.89358	8.88	8.73	8.97	13.88	-19.16	28.53	18.46	2.47	45.72
4040	53.05832	-27.88487	9.00	8.94	9.12	12.49	-20.42	27.58	49.74	2.46	48.20
6802	53.03079	-27.89739	9.18	8.99	9.59	4.03	-18.11	29.36	8.47	2.50	25.50
9101	53.06774	-27.86455	9.24	9.15	9.97	16.34	-18.57	29.18	11.60	2.30	71.47
3908	53.09749	-27.85678	9.29	9.23	10.30	8.82	-18.13	29.23	10.85	2.47	38.19
13097	53.07477	-27.84543	9.40	9.28	9.79	6.47	-18.21	29.68	7.22	-1.00	-1.00
4277	53.09747	-27.85698	9.40	9.34	9.96	4.96	-18.72	29.18	11.47	2.30	66.06
2883	53.09871	-27.86018	9.59	9.52	10.26	13.01	-17.97	29.55	7.17	2.47	39.27
10045	53.07608	-27.85602	9.64	9.58	10.29	7.07	-18.27	29.37	9.20	2.30	47.92
9634	53.08537	-27.85047	9.67	9.54	10.00	10.93	-18.17	29.67	5.93	2.31	49.81
13136	53.06020	-27.85627	9.72	9.34	10.01	5.68	-18.06	30.05	5.57	2.28	39.84
15021	53.01654	-27.88196	10.15	9.56	10.33	12.49	-18.37	29.60	8.44	2.35	60.32
1680	53.06005	-27.89143	11.15	10.77	11.50	19.09	-18.04	30.10	5.96	0.03	40.09
11825*	53.02617	-27.88717	11.40	11.04	11.68	14.38	-18.04	30.06	5.33	0.06	34.56
3217	53.07803	-27.87366	12.16	11.99	12.37	28.63	-18.71	29.12	9.69	3.29	43.09
8885*	53.02867	-27.89301	12.25	12.11	12.59	24.04	-18.86	29.50	9.65	3.26	45.56
922*	53.06474	-27.89023	12.93	12.79	13.17	15.16	-18.64	29.40	10.19	3.53	58.38
730*	53.10762	-27.86012	14.91	14.65	15.74	11.45	-18.56	29.62	7.47	4.17	26.16
9751	53.03491	-27.88335	7.55	7.22	7.57	31.39	-17.68	30.39	5.09	0.26	50.11
1181	53.05564	-27.89547	7.86	7.80	7.93	37.80	-17.50	29.97	7.86	1.50	50.05
10018	53.09278	-27.84107	7.87	7.16	7.92	22.55	-17.63	30.04	7.78	1.50	67.79
6610	53.07575	-27.86352	7.88	7.80	7.95	25.79	-16.95	30.34	5.33	2.36	33.64
12634	53.04504	-27.86981	8.13	7.96	8.26	29.07	-17.95	29.24	16.19	1.75	33.55
5178	53.03769	-27.89540	8.17	8.10	8.29	9.88	-17.71	29.72	9.14	1.72	31.03

11523	53.07259	-27.85059	8.18	8.01	8.32	26.47	-17.91	29.75	7.29	0.23	90.41
9814	53.04759	-27.87403	8.24	8.11	8.39	8.50	-17.53	30.16	5.66	0.09	48.69
11293	53.06709	-27.85541	8.25	7.87	8.36	37.89	-17.58	30.09	5.97	-1.00	-1.00
548	53.04853	-27.90285	8.27	8.00	8.34	33.85	-18.57	30.02	7.26	1.92	39.71
10790	53.08439	-27.84471	8.30	8.13	8.47	20.44	-17.58	29.95	8.10	0.24	45.10
2273	53.09058	-27.86704	8.32	7.97	8.40	23.64	-18.09	30.04	8.57	2.12	28.81
3819	53.09083	-27.86177	8.41	8.25	8.54	5.96	-18.28	29.11	14.52	1.99	31.29
3563	53.05173	-27.89058	8.56	8.23	8.65	29.79	-17.30	29.65	12.81	1.93	35.60
8308	53.06697	-27.86450	8.65	8.56	8.86	21.08	-17.16	29.72	10.98	0.30	25.85
6705	53.07755	-27.86198	8.76	8.59	9.05	22.88	-18.42	29.86	5.90	2.11	31.18
6730	53.05615	-27.87735	8.77	8.65	9.02	27.73	-17.41	30.13	7.55	0.20	33.98
4817	53.04858	-27.88875	8.85	8.68	9.05	27.06	-17.64	30.44	5.14	1.96	43.91
5867	53.07900	-27.86358	9.26	9.08	9.43	26.58	-18.02	29.79	9.23	0.21	32.52
6312	53.09208	-27.85278	9.40	9.35	10.40	9.57	-18.11	29.41	13.00	2.36	26.81
2961	53.05681	-27.88898	9.56	9.49	10.01	19.88	-17.58	30.15	7.06	2.31	62.55
4253	53.04887	-27.89045	10.18	9.71	10.48	6.50	-17.98	29.73	9.81	2.49	39.66
13111	53.07207	-27.84174	10.80	10.56	10.99	10.68	-18.41	30.20	6.23	2.31	73.68
10118*	53.07248	-27.85535	11.25	10.90	11.39	17.22	-17.84	29.38	14.83	3.04	62.57
3653	53.08716	-27.86492	12.18	11.89	12.33	15.88	-17.68	29.62	10.01	3.30	27.11
3654*	53.08468	-27.86667	12.84	12.60	13.65	14.51	-17.86	29.65	8.65	3.52	20.70
12407	53.04293	-27.87044	13.46	12.61	13.73	18.29	-18.02	29.86	8.99	3.58	22.84
7891	53.02638	-27.89487	15.93	15.77	16.06	33.48	-18.06	30.11	6.36	4.17	42.16
908	53.10041	-27.86442	17.33	17.21	18.90	10.32	-18.04	30.42	5.95	5.05	66.40

Notes: * indicates object was selected in [Robertson et al. \(2024\)](#)

This paper has been typeset from a $\text{\TeX}/\text{\LaTeX}$ file prepared by the author.

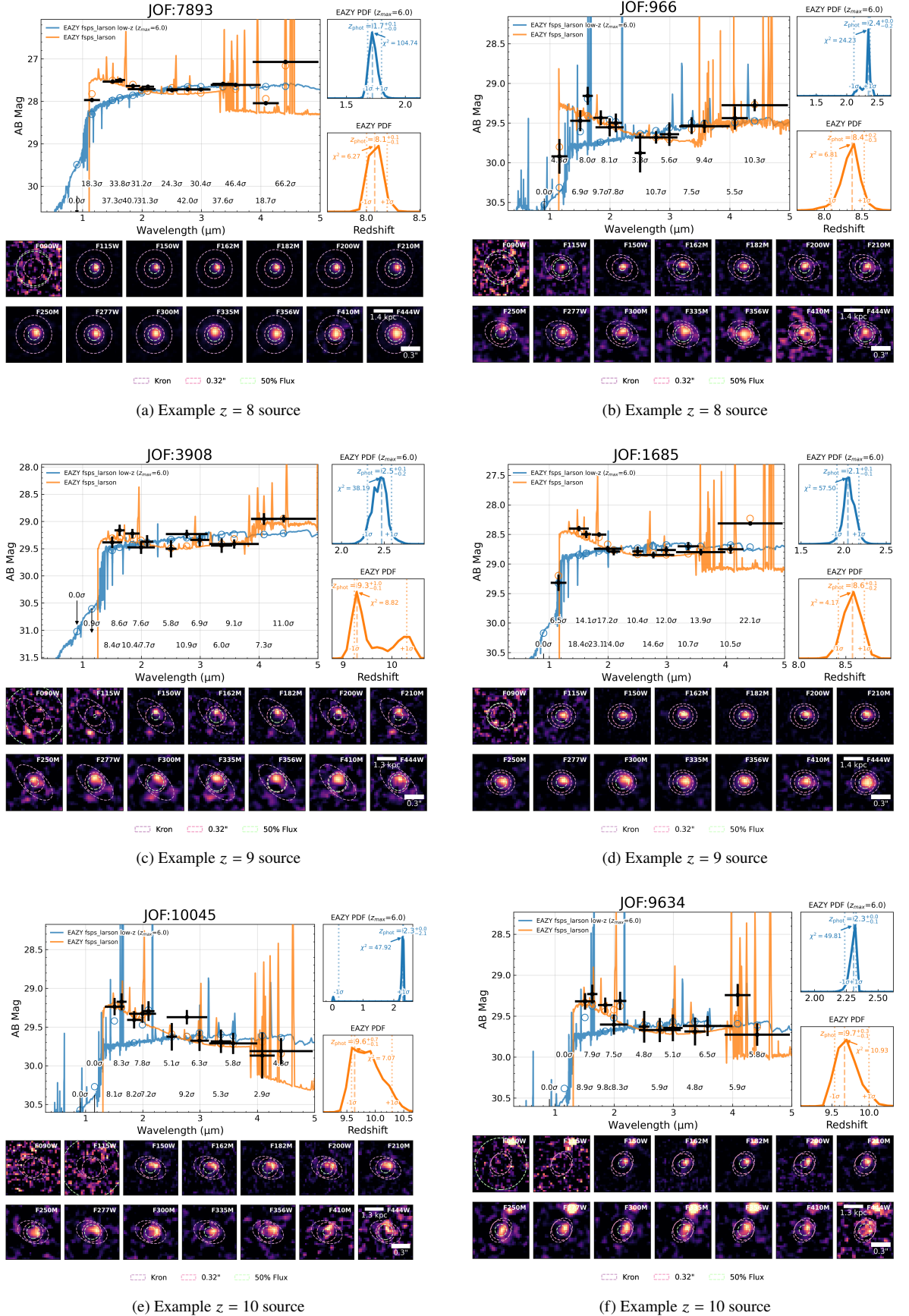
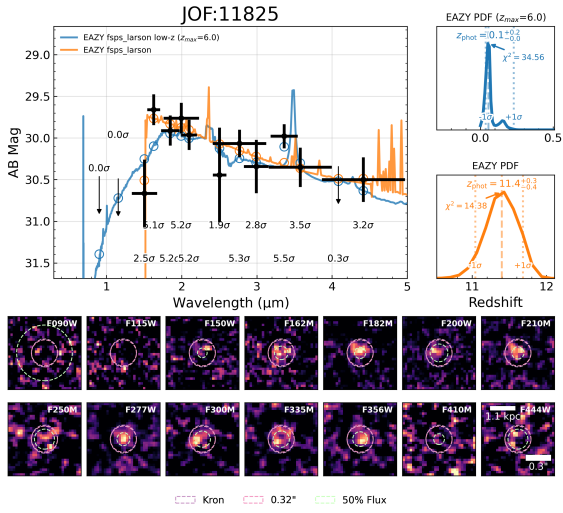
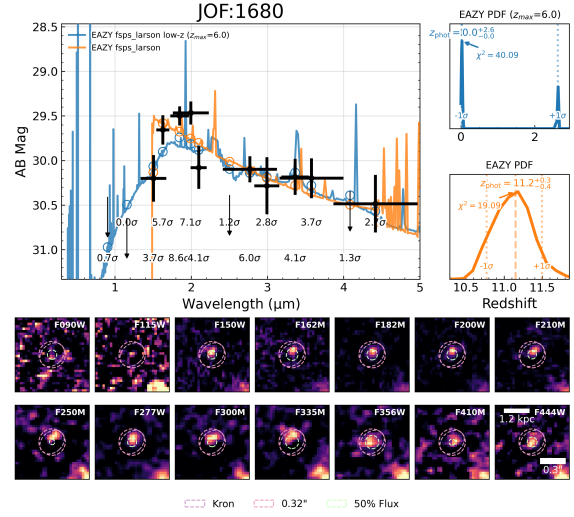


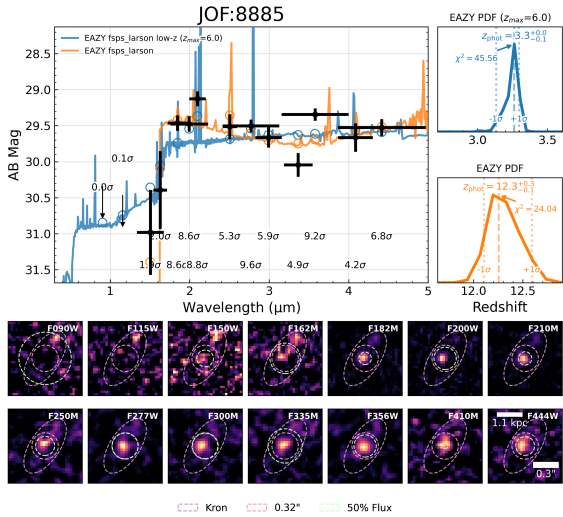
Figure A1. A random selection of example SED fits for objects selected between $7.5 < z < 13.5$. Orange lines show the best high- z fit while the blue lines show the next best low- z fit at $z < 6$, these are typically Balmer breaks or 1.6 micron bumps.



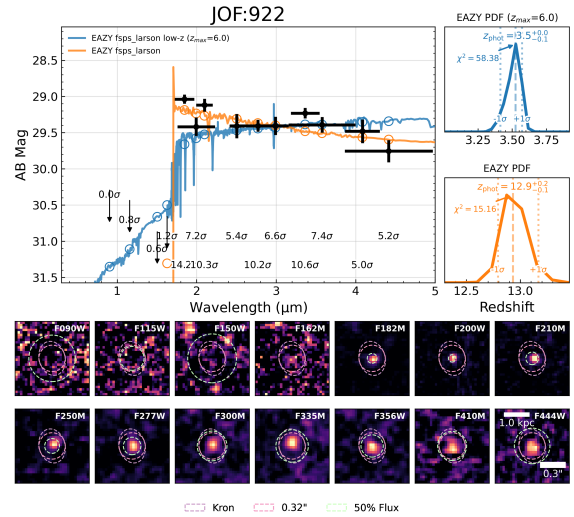
(g) Example $z = 11$ source



(h) Example $z = 11$ source



(i) Example $z = 12$ source



(j) Example $z = 13$ source

Figure A1. A random selection of example SED fits for objects selected between $7.5 < z < 13.5$. Orange lines show the best high- z fit while the blue lines show the next best low- z fit at $z < 6$, these are typically Balmer breaks or 1.6 micron bumps.